NASA Technical Memorandum 78532

Symmetrical and Asymmetrical Separations About a Yawed Cone

David J. Peake, F. Kevin Owen, and Hiroshi Higuchi

September 1978

National Aeronautics and
Space Administration

NASA Technical Memorandum 78532

Symmetrical and Asymmetrical Separations About a Yawed Cone

David J. Peake, Ames Research Center, Moffett Field, California 94035
F. Kevin Owen, Owen International Inc., Palo Alto, California 94302
Hiroshi Higuchi, Dynamics Technology Inc., Torrance, California 90503

NASA
National Aeronautics and
Space Administration

Ames Research Center
Moffett Field, California 94035

SYMMETRICAL AND ASYMMETRICAL SEPARATIONS ABOUT A YAWED CONE

David J. Peake
Senior NRC Research Associate
Ames Research Center, NASA
Moffett Field, California 94035, U.S.A.

F. Kevin Owen
Consultant, Owen International Inc.
Palo Alto, California 94302, U.S.A.

Hiroshi Higuchi
Research Scientist, Dynamics Technology Inc.
Torrance, California 90503, U.S.A.

SUMMARY

Three-dimensional flow separations about a 5° (semiapex angle, θ_c), 1.4-m (54-in.) long, circular cone up to moderately high relative incidences, $\alpha/\theta_c \sim 5$, have been investigated in the Mach number range $0.6 < M_\infty < 1.8$. The cone was tested in the Ames 1.8- by 1.8-m (6- by 6-ft) Wind Tunnel at Reynolds numbers, R_{L_∞}, based on the cone length, L, from 4.5×10^6 to 13.5×10^6, under nominally zero heat transfer conditions. Overall forces and mean surface pressures were compared with earlier measurements made in the NAE Ottawa 1.5- by 1.5-m (5- by 5-ft) Blowdown Wind Tunnel, where $R_{L_\infty} \sim 35 \times 10^6$.

The lee-side separated flow develops from initially symmetrically disposed and near-conical separation lines at $\alpha/\theta_c \sim 1$, with the free shear layers eventually rolling up into tightly coiled vortices at all Mach numbers. At Mach 0.6, conditions in this symmetrical external separated flow at $\alpha/\theta_c = 2.5$, were probed with pitot pressure tubes and optically via laser/vapor screen flow visualization. Mean shear stresses and directions on the cone surface were inferred from a previously calibrated pair of yawed hot wires, while fluctuations at the surface were measured by the hot wires and pressure transducers, as the cone was rolled in small increments through separation.

The onset of asymmetry of the lee-side separated flow about the mean-pitch plane is sensitive to Mach number, Reynolds number, and the nose bluntness, varying between $2.5 < \alpha/\theta_c < 4.5$ in the Mach number range $0.6 < M_\infty < 1.8$. As the Mach number is increased beyond $M_\infty = 1.8$, the critical angle of incidence for the onset of asymmetry increases until at about $M_\infty = 2.75$ there is no longer any significant side force development.

Supportive three-dimensional laser velocimeter measurements of mean and fluctuating velocity in a slightly asymmetric vortex wake about a slender tangent ogive cylinder at incidence having respective nose and overall body fineness ratios of 3.5 and 12, are included. These measurements were obtained at $\alpha/\theta_c = 2.3$; at Mach 0.6; and at $R_{L_\infty} = 2 \times 10^6$, where L = 0.3 m (1 ft).

SYMBOLS

A	a constant, see Eq. (1)
B	a constant, see Eq. (1)
$C_f = \frac{\tau_w}{q_\infty}$	local resultant skin friction coefficient
C_N	normal force coefficient from balance, based on cone base area
$C_p = \frac{p-p_\infty}{q_\infty}$	local static pressure coefficient
$C_{pp} = \frac{p_p-p_\infty}{q_\infty}$	local pitot pressure coefficient
C_Y	side-force coefficient from balance, based on cone base area
D	base diameter of cone
d	diameter of tangent ogive/cylinder model
d_p	diameter of vent port to pressure transducer beneath cone surface
E	mean operating voltage of hot wire, flow on
E_0	mean operating voltage of hot wire, flow off
e', e(t)	instantaneous fluctuation voltage from hot wire
<e'>	rms voltage from hot wire
h	height above cone surface, measured along extended radius of cone

$\bar{h} = \frac{h}{r}$ nondimensional height above cone surface

K a constant, see Eq. (1)

L axial length of cone

M local Mach number

p local static pressure

p' instantaneous level of pressure fluctuation at cone surface

<p'> rms of pressure fluctuation at cone surface

p_p local pitot pressure

q local dynamic pressure

R ohmic resistance

$\Delta R = (R_{op} - R_w)$ difference between resistances of a wire at, respectively, operating temperature and local wall temperature

R_{L_∞} Reynolds number based on axial length of cone and tunnel free-stream conditions

r local cone radius

S electrical "power" term, defined in Eq. (2)

t time

t_D time delay

u local velocity in direction of tunnel axis

$\tilde{u}$ local velocity, parallel to model axis

$u_\tau = \sqrt{\frac{\tau_w}{\rho_w}}$ shear stress velocity

v lateral velocity normal to tunnel or model axis

w vertical velocity normal to tunnel axis

$\tilde{w}$ vertical velocity normal to model axis

x distance along tunnel axis

$\tilde{x}$ distance along model axis

y lateral distance from tunnel or model axis

z vertical distance, normal to tunnel axis

$\tilde{z}$ vertical distance, normal to model axis

α angle of incidence

δ boundary-layer displacement thickness

θ angle between local shear stress vector and line bisecting internal angle between individual wires of buried wire skin — friction gage, see Fig. 4(a)

θ_c cone semiangle

μ coefficient of viscosity

$\nu = \frac{\mu}{\rho}$ kinematic viscosity

ρ local density

τ mean shear stress

τ' instantaneous level of shear stress fluctuation at cone surface

ϕ circumferential angle around cone surface, measured from windward generator

ψ angle between normal to buried wire and local surface shear stress direction, Fig. 5(a)

ω	angle between tangent to limiting streamline (surface shear stress trajectory) and cone generator

Subscripts:

1,2	wires 1 and 2 of buried wire gage, see Fig. 4(d)
A	line of divergent surface shear stress trajectories ("attachment" or "reattachment" line)
b	cone base
∞	free-stream mean-flow conditions
op	operating temperature of hot wire
S1	primary separation line
S2	secondary separation line
w	cone surface (wall)

1. INTRODUCTION

1.1 Design Aims

To be successful throughout a wide range of flight conditions, the aerodynamic design of a lifting body must ensure that there is adequate control with no unpleasant changes in force and moment characteristics. In association with steady boundary conditions, the objective is to allow only steady three-dimensional swept separations to develop, to minimize buffet. A model for a desirable separated flow is provided by the sharp-edged slender delta wing or a body of revolution with fixed separation lines (Ref. 1). In aiming for this ideal goal, we find that flows should be dominated by coiled vortices — "the sinews and muscles of fluid motion" (Ref. 2) — rather than by large unsteady separation bubbles. This much wider than usual view of the aerodynamic design problem, attributable to Maskell and Küchemann (Ref. 3), should be contrasted with the restricted outlook of allowing separation only at a trailing-edge, as in the design of the classical airplane.

1.2. Asymmetric Separations

Our present-day missiles and military fighter aircraft must perform and be controllable at high angles of combined incidence and yaw, where three-dimensional flow separations from the forebodies may become asymmetric (Refs. 4-7). These separations, often in association with fixed-edge separations from strakes extending forward of the wing, may interfere with downstream control surfaces to provide nonlinearities and side forces that are not readily predictable. Here there is strong interaction between the coupled viscous and inviscid flow domains on the lee-side of the vehicle. The onset of asymmetry is responsive to small changes in geometry at the nose, Reynolds number and Mach number up to incidences where transonic crossflow conditions are formed. There the significant side forces disappear. The asymmetries occur in both laminar and turbulent flows, so that transition is presumably not the essential ingredient causing asymmetry. But local inflexional instability of the mean velocity profiles in the viscous flow may, perhaps, be mooted as a contributor (see Tobak's discussion, Ref. 8, of a linearized theory of two- and three-dimensional incompressible viscous flows resulting from locally unstable velocity profiles). It is conceivable that vorticity and acoustic disturbance levels in the wind tunnel will also affect the onset of asymmetry. As the development of the asymmetry is particularly sensitive to surface curvature and roughness at the nose, a potential means of controlling the forebody flow could be by deployment of a single small strake, small amounts of asymmetric blowing (or suction), or by spinning the nose. On the other hand, since we know that missiles having long cylindrical afterbodies will eventually develop asymmetrical flows regardless of nose conditions, we might be led to expect that such local treatment at the nose would probably not influence the downstream flow substantially. Notwithstanding, Rao (Ref. 9) has demonstrated that the utilization of helical (i.e., S-shaped) trip wires from the leeward to the windward meridian on the nose, disrupts the normal development of separation, and is very effective in alleviating high angle-of-attack side forces on short missile and fuselage shapes. It is considered that the helical trips upset the well-organized motion of the lee-side vortices and cause a relatively rapid diffusion.

The asymmetric vortex wake usually develops from asymmetric separation line positions on the body, but the latter does not appear to be a necessary condition for the former to occur. An appraisal (Ref. 10) of some earlier, low subsonic speed tests of Shanks (Ref. 11) where forces and moments were measured on very slender, flat plate, delta wings (sweep angles from 70° to 84°) at incidence, indicates that even though the separation lines were fixed at the sharp leading-edges, asymmetry in the leading-edge vortices, as determined by the onset of significant rolling moment, occurred when the angle of incidence was about 3 to 4 times the wing seminose angle. Nonetheless, the sharp edges have a beneficial effect in delaying the onset of asymmetry to higher relative incidences than those obtained with smooth pointed forebodies or forebody/cylinder configurations (Refs. 5-7).

1.3. Modeling of Asymmetries

The modeling of the lee-side flow asymmetries poses severe problems because the development of the turbulent flow structures in the three-dimensional swept separation zones and in the tightly coiled free shear layers is virtually unexplored. Recourse has typically been taken for rough predictions of the flows about missile shapes, to inviscid flow approximations of the lee-side region utilizing arrays of line-vortices (see Nielsen's review in Ref. 12 of nonlinearities in missile behavior at high angles of attack), or to the impulsively started flow analogy proposed many years ago by Allen and Perkins (Ref. 13). In this hypothesis, the development of the crossflow with distance along an inclined body of constant diameter is likened to the growth with time of the two-dimensional flow past the corresponding circular cylinder starting impulsively from rest. Useful engineering formulae have resulted, but given the complexities of the three-dimensional boundary-layer growth, separation, and vortex development on slender bodies, it seems unlikely that methods of this kind can adequately describe the flow. In general, we should note that the growth of the unsteady two-dimensional spiraling vortex differs essentially from that of the steady, three-dimensional vortex in space. Küchemann and Weber (Ref. 14) point out that in three dimensions, fluid entering the core of the vortex can be discharged axially, whereas in two dimensions no such escape is available. The core must expand continuously outward with time to accommodate all of the fluid entering the vortex. They show further (Ref. 14) that there is only one case in inviscid flow where the two kinds of vortex are formally identical: where the steady, three-dimensional flow is conical (so that slenderness assumptions can be invoked); and where the unsteady flow is permitted to grow linearly with time. Lamont and Hunt (Ref. 15) and Deffenbaugh and Koerner (Ref. 16) have probably extracted the limits of usefulness of the qualitative, two-dimensional, unsteady analogue to describe the nature of "out-of-plane" forces on a pointed body at high angles of incidence.

1.4. Cone at Incidence (or Yaw) — A Simple Model of Three-Dimensional Separation

Next to the slender delta wing, the simplest class of bodies on which three-dimensional separation can be studied is the cone. As well as being a typical forebody shape used in flight, the cone at incidence provides a very useful model to develop three-dimensional boundary layers, up to and beyond separation, to check against theory. On a conical surface, the condition for flow separation is simple; namely, that the limiting streamlines at the base of the skewed boundary layer (whose projections on to the surface are the directions of surface shear stress) coalesce from both sides to form an envelope (Refs. 17, 18) along, or are asymptotic (Refs. 19, 20) to, a cone generator. Even in incompressible flow about slender cones, the conical nature of the surface conditions with separation is preserved. This is because at relative incidences sufficient to cause separation, the circumferential pressure gradients are much larger than those in the axial sense (the latter due to thickness and base effects). For the incompressible case as well, then, the primary separation line lies essentially along a generator as illustrated by the limiting streamlines in laminar flow about a 1.5:1 elliptic cone with major axis vertical at 30° incidence (Ref. 21), shown in Fig. 1.

1.5. Computation of the Symmetrical Lee-side Flow about Cones

The computation of the symmetrical separated lee-side flow about cones is currently following two paths. One is the representation of the cone flow by parabolized approximations to the Navier-Stokes equations in supersonic flow (Refs. 22-24); the second is the inviscid modeling in incompressible flow of the free shear layers by spiral vortex sheets as for delta wings (Ref. 25).

McRae (Ref. 22) incorporated the conically symmetric flow approximation along with MacCormack's finite-difference time-dependent scheme (Ref. 26) to solve the laminar viscous flow field about a pointed circular cone. The calculation takes place on a spherical surface centered on the cone apex. The outer boundary condition for the integration is the free stream, so that the bow shock wave is captured and allowed for in the use of the conservative form of the governing equations. A comparison with the Mach-8 surface pressure and pitot measurements of Tracy (Ref. 27) showed good agreement with the calculations of the lee-side flow. McRae (Ref. 23) has now included a scalar eddy-viscosity model based on mixing-length hypotheses in his formulation. Provided certain constants are used to adjust the levels of eddy viscosity in each coordinate direction, coupled with relaxation beginning just prior to the primary separation, he finds very satisfactory agreement between his calculations of surface pressure and surface shear stress directions and the results of the high Reynolds number experiments of Rainbird (Refs. 28, 29). Both primary and secondary separation line positions were found to agree very closely with experimental results in a Mach 1.8 flow at $\alpha/\theta_c = 2.5$ and $R_{L_\infty} \sim 30 \times 10^6$.

Rakich and Lubard (Ref. 24) calculated the entire laminar separated flow field about a spherically blunted 15° circular cone in a Mach 10.6 flow to compare with the measurements of Cleary (Ref. 30) at $\alpha/\theta_c \sim 1$. The calculations are based on a single layer system of three-dimensional parabolic equations that are approximations to the full steady Navier-Stokes equations valid from the body surface to the bow shock wave. This system of equations includes the circumferential shear stress terms as well as the effects of viscous-inviscid interaction and entropy gradients due to both the curved bow shock and angle of attack. The calculated leeward surface pressures and heating distributions were in satisfactory agreement with experimental results and the calculation provided evidence of reversal in the boundary-layer crossflow; primary separation was placed at about 13° from the leeward meridian. The results from a variant of this program (Ref. 31), wherein an eddy viscosity model is inserted are also being compared against Rainbird's Mach 4.25 experiments (Ref. 29).

Pulliam and Steger (Ref. 32) have also made a notable contribution to the calculation of flows about missile-shaped bodies using a "thin layer" approximation of the Navier-Stokes equations.

The second avenue of modeling the lee-side vortex wake, in this case, by wholly inviscid means, is that due to J. H. B. Smith (Ref. 25). He proposes an inviscid vortex sheet model for incompressible (symmetrical, at this time) conical flow in which the vortex sheet must depart from the surface of the cone tangentially if vorticity is to be shed. The separation line position may be given from boundary-layer calculations (see Smith's review (Ref. 33) in AGARD CP-168) or from experiment (see Fig. 2). At the separation line in Smith's model, the inviscid flow on the downstream side is constrained to be parallel with the separation line, a condition to replace the Kutta condition at a sharp edge; whereas on the upstream side of the separation line, the surface streamlines of the inviscid model are inclined to the separation line (but are, of course, tangential to the wall). The coiled inviscid vortex sheet is then constructed as for the sharp-edged delta wing (Refs. 39, 40).

1.6 Cone for Experiment

The cone, then, is the basic nose of many flight vehicles. At incidences typically below $\alpha/\theta_c \sim 1$, it provides a useful configuration to develop a symmetrical three-dimensional attached boundary layer growing from the windward to the leeward meridian. Because of the near conicity of the separation lines and vortex development in both subsonic and supersonic flows (neglecting effects of transition), it also provides a convenient experimental model to explore three-dimensional separations from detailed measurements at only one axial station.

The essential objective of the present work is to achieve an understanding of the fluctuating quantities in three-dimensional separated flows, and how three-dimensional separations and their asymmetries may be controlled. The cone is a very convenient model on which to generate both three-dimensional attached and separated viscous flows. The present experiments then, extend the symmetric separation mean flow measurements of Rainbird (Refs. 28, 29) about circular cones (see also Ref. 41) to determine experimentally additional quantities at the cone surface (mean and fluctuating pressures, fluctuating heat transfer combined with mean shear stress magnitudes and direction) and to measure at the same time the mean and fluctuating flow field above the cone at moderately large relative incidence. Test results at Mach 0.6 are discussed herein. Force measurements in the range of Mach number $0.6 < M_\infty < 1.8$ have yielded the onsets of asymmetry of the lee-side flow for varying Reynolds numbers and for blunt and sharp nose shapes. These were supplemented herein by pictures of the crossflow facilitated by a laser-vapor screen flow visualization technique.

2. EXPERIMENTAL METHOD

Measurements have been made on a 1.4 m (54 in.) long, 5° semiangle circular cone, sting-mounted in the Ames 1.8- by 1.8-m (6- by 6-ft) closed circuit wind tunnel at Mach numbers in the range $0.6 < M_\infty < 1.8$ (Fig. 3). The cone model was fitted with a sharp nose (0.13-mm, i.e., 0.005-in. tip radius) and a blunted nose with a radius of 4% of the base radius. Stagnation pressures were subambient yielding Reynolds numbers based on the cone axial length and tunnel free-stream conditions of between 4.5×10^6 and 13.5×10^6. No artificial tripping of the boundary layer was employed. At the relatively high acoustic disturbance levels pertaining in this tunnel, for example, $\langle p' \rangle / q_\infty \sim 3\%$ at $M_\infty = 0.6$, a Reynolds number based on wetted length to transition might be expected to be $3 \times 10^6 \pm 20\%$ (Ref. 42). At zero angle of attack, therefore, we anticipate transition to have been located, respectively, from about 0.7 to 0.2 of the cone length, corresponding with the aforementioned range of test Reynolds numbers with a tunnel stagnation temperature in the range of 20°-40°C. The typical variation during a run of 20 min was less than 3°, however, so that with this immersion time, conditions of near zero heat transfer existed at the cone surface.

Because of the nominal conicity and symmetry of the flow (Refs. 4, 28, 29) up to angles of incidence at least 2.5 times the nose semiangle, θ_c, all detailed measurements were made at an axial station 0.85 of the cone length aft of the (pointed) apex and upon each half of the cone ($0° < \phi < \pm 180°$). Mean circumferential pressure distributions were obtained with 0.51-mm (0.020-in.) diameter static holes spaced 45° apart at the 0.85 station (see Fig. 4(a)). These orifices, as well as others along a cone generator at the 0.95 station and in the base region, were connected via a "Scanivalve" to an unbonded strain-gage pressure transducer. The static pressure from each point at the 0.85 station was also fed as a highly damped signal to the reference port of a 2.36-mm (0.093-in.) diameter "Kulite" pressure transducer situated on the same conical generator. The diaphragm was vented to the flow through a 1.00-mm (0.040-in.) diameter static hole but submerged beneath the surface in accordance with Hanly's recommendations about the effects of transducer flushness on fluctuating surface pressure measurements (Ref. 43) (see Fig. 4(b)). Preston tubes of diameter 0.42 mm (0.016 in.) were installed at the 0.85 station to determine the mean levels of skin friction at zero angle of attack and along the windward generator (Fig. 4(c)).

Two bidirectional, buried-wire, skin-friction gages (Ref. 44) were also situated in the cone surface at the 0.85 length station (see Fig. 4(a)), to measure the magnitude and direction of the resultant shear stress at the surface. The configuration of the gage is shown in Fig. 4(d), its fabrication following basically the same procedure as promoted for single wires by Murthy and Rose (Ref. 45) after the work of Rubesin et al. (Ref. 46). The following equations, the method of manufacturing the gages, and a full discussion of the calibrations are given in Ref. 44. In brief, temperature-resistance calibrations were obtained by placing the gages in an oven. Magnitude and directional sensitivities were found by flush-mounting the gages in a known subsonic channel flow and operating each wire with an overheat ratio of 1.1, utilizing "Disa" constant temperature anemometers. The wires were capable of operating with upper frequency responses close to 15 kHz. The sensitivities were checked again after installation in the cone surface and running at zero angle of attack. The shear stress at a station close by the gage was deduced from a Preston tube measurement in conjunction with the correlation due to Bradshaw and Unsworth (Ref. 47). Rotation of the probe about its axis to known angles of yaw permitted the directional sensitivity to be obtained at each Mach number and Reynolds number tested simultaneously with the shear stress magnitude according to the following equations. If the output of a single wire, yawed to the local shear stress direction at $(90 - \psi)°$ (see Figs. 4(d) and 5(a)), is assumed to be of the form:

$$\frac{E^2}{R\Delta R} = A(\rho_w \mu_w \tau_w)^{1/3} (\cos^2 \psi + K^2 \sin^2 \psi)^{1/6} + B \qquad (1)$$

where the symbols are defined at the beginning of the report, and

$$S = \frac{1}{A}\left(\frac{E^2}{R\Delta R} - B\right) \tag{2}$$

then for our pair of mutually perpendicular wires, respectively labeled 1 and 2, where $\psi_1 + \psi_2 = \frac{\pi}{2}$, we obtain

$$S_1 = (\rho_w \mu_w \tau_w)^{1/3} \left(\cos^2 \psi_1 + K_1^2 \sin^2 \psi_1\right)^{1/6} \tag{3}$$

and

$$S_2 = (\rho_w \mu_w \tau_w)^{1/3} \left(\sin^2 \psi_1 + K_2^2 \cos^2 \psi_1\right)^{1/6} \tag{4}$$

By eliminating ψ_1, the wall shear stress is given by

$$(\rho_w \mu_w \tau_w) = \left[\frac{(1 - K_2^2)S_1^6 + (1 - K_1^2)S_2^6}{1 - K_1^2 K_2^2}\right]^{1/2} \tag{5}$$

We note that values of the coefficients of directional sensitivity K_1 and K_2 can be obtained from a plot of $S_1(\psi_1)$ or $S_2(\psi_2)$ when $\psi_1, \psi_2 = 0°$. In general, $K_1 \neq K_2$, but the difference between the two sensors on each gage was found to be relatively small. If, for simplicity, we let $K_1 = K_2 = K$, then the absolute magnitude of the shear stress takes the form:

$$(\rho_w \mu_w \tau_w) = \frac{(S_1^6 + S_2^6)^{1/2}}{(1 + K^2)^{1/2}} \tag{6}$$

As for the direction of the skin friction vector, we see from Eqs. (3) and (4) that the quotient S_1/S_2 is a unique function of the direction ψ_1 and is independent of the magnitude of the skin friction. The assumption $K_1 = K_2$ is not a necessary one provided each wire of a pair is calibrated. McCroskey and Durbin (Ref. 48) discussed measurements of the direction of surface shear stress with a hot film gage and proposed that

$$\frac{S_1 - S_2}{S_1 + S_2} = f(\theta) \tag{7}$$

where θ is the direction of the flow relative to the probe centerline, and equals $(\psi_1 - \pi/4)$ in our present frame of reference.

The results of the directional calibration for one of the pairs of buried wires is shown in Fig. 5(a). We see that the direction of the skin friction vector can be determined to an accuracy within ±5° independently of its magnitude. The variation of the quantity $(S_1^6 + S_2^6)^{1/2}$ in a ±40° yaw angle range was demonstrated to be small. The magnitude of skin friction obtained with the Preston tube is plotted against the measured values of $(S_1^6 + S_2^6)^{1/2}$ in Fig. 5(b). From Eq. (6), the value of K is 0.35 for the particular gage shown. The surface shear stress directions obtained with the hot wire pair were compared against flow visualization traces taken with an oil-dot technique. Signals from the off-surface hot wires were also measured but await analysis.

Pitot pressures in the external flow above the cone surface were measured using an array of 77 pitot tubes mounted at the 0.85 station (Fig. 3).

Overall force and moment measurements were obtained with an internal strain-gage balance.

The cone was pitched to the desired angle of incidence, and for the measurements with symmetrical separation of the lee-side flow, the cone was rolled in increments from 0° to 180° and paused for typically 1 min while data were taken. Increments of 5° in roll were generally used. Neither fluctuating pressures nor hot wire data were collected at angles of incidence where asymmetric lee-side conditions prevailed.

Visualization of the vortex wake was obtained at the 0.85 station by saturating the tunnel flow with water vapor and illuminating a thin cross section of the flow with a 15-W laser beam passed through a cylindrical lens. Photographs of the scattered light were taken with a camera mounted to the sting/strut support, the camera axis being set nominally parallel with the cone surface. Prior to the runs, a grid placed at the test station was photographed against which the dimensions of the shear layer could be subsequently compared.

Some supportive three-component velocity measurements in the lee-side vortex wake just downstream of the junction between a 16° semiangle tangent ogive forebody joined to a cylinder aft-body were made by Owen and Johnson (Ref. 49) at a relative incidence of 2.3. These Mach 0.6 data are also presented here to provide an insight into possible orders of magnitude of fluctuation levels on the lee side of the cone.

3. RESULTS AND DISCUSSION

3.1 Symmetrical Separation of the Lee-Side Cone Flow

3.1.1 Forces

The physical characteristics of the mean flow field about the 5° circular cone in the Mach number range $0.6 < M_\infty < 1.8$ follow the descriptions by Rainbird (Refs. 28, 29) of the surface and external flow conditions that he measured at Mach 1.8 and 4.25.

The overall effects of boundary-layer growth and incidence on the development of normal forces on the 5° cone are illustrated in Fig. 6 up to relative incidences of almost 5. At relative incidences typically less than 0.7, the circumferential pressure gradient is favorable all the way from the windward to the leeward generator. The boundary layer grows in a regular manner developing very small crossflows. The normal force develops linearly in this range, and the slopes $dC_N/d\alpha$ near $\alpha = 0°$, are affected only slightly by viscosity. In subsonic flow, the values are typically 6% larger than the slender body value of 2.0 (per radian). In supersonic flow, the discrepancies between experiment and those slopes given in Sims' tables (Ref. 50) are even less for both the blunt and sharp noses.

Figure 6 illustrates that, at Mach 1.8, there is substantial development of nonlinear lift* above a relative incidence of 1.5 (as found by Rainbird (Ref. 28), where the Reynolds number was more than double the existing test value) consistent with the formation of a well organized, symmetrical, coiled, free shear-layer flow on the lee side of the model. From pitching-moment data, a fixed center of pressure position at 0.667 L is in good agreement with the conical flow value of $(2/3)L \sec^2 \theta_c$. But below Mach 1.8, there is an apparent sensitivity of the onset of nonlinear normal force to both Reynolds number and nose shape, as we see on Fig 7. At any given Mach number, we note that reduction in Reynolds number and introduction of bluntness delays the onset of nonlinear normal force. This dependency reduces rapidly as Mach number increases until at Mach 1.8, it has nominally disappeared.

The results in Fig. 7 for our cone model of fineness ratio, L/D = 5.7, are unexpected for the distinctive tardiness displayed in producing nonlinear normal force in the high subsonic and transonic speed ranges. Even though at Mach 0.6 and $\alpha/\theta_c \sim 2.5$, for example, where there was substantial vortex flow (see Figs. 8 and 9), the overall normal force lies just below the slope $(dC_N/d\alpha)_{\alpha=0}$.

The high negative values of base pressure coefficient (Fig. 10), are mooted as the key to the paradox, for at $M_\infty = 0.6$ near the base, they induce somewhat larger increments of suction pressure on the windward side of the cone near the base than on the leeward; see for example, the cone surface pressures along the windward and leeward generators on Fig. 11. Hence the development of nonlinear normal force appears suppressed by the base effect. This suppression reduces as Mach number increases until at $M_\infty \sim 1.8$, the upstream propagation from the base is negligible.

In Fig. 10, we also note that changes in Reynolds number and sting/base diameter at Mach 0.6 cause substantial changes of the base flow (see Ericsson (Ref. 53) for a discussion on aerodynamic support interference).

3.1.2 Mean Flow Measurements

The changes in three-dimensional boundary-layer development as the circumferential surface pressure distributions steepen with increasing angle of incidence are discussed in detail in Refs. 28 and 29. Herein, we shall concentrate on the flow at a relative incidence of 2.5, for the cone with nose radius equal to 4% of base radius. At this incidence (Figs. 12(a)-12(c)), display the surface pressure coefficients obtained at a constant length Reynolds number of $R_{L_\infty} = 13.5 \times 10^6$, for Mach numbers 1.8, 1.2, and 0.6. The pressures are plotted with respect to circumferential angle measured from the windward ($\phi = 0°$) to the leeward generator ($\phi = 180°$). Figure 12(a) shows good agreement at $M_\infty = 1.8$ between the measured circumferential pressures plotted at three axial stations along the cone. The present results at $R_{L_\infty} = 13.5 \times 10^6$ demonstrate a small but variable shift relative to the higher Reynolds number data of Refs. 28 and 29. The present results are uncorrected for errors due to static hole size (Refs. 54, 55) which, if included, would marginally increase the difference between the two sets of measurements. The calculation of surface pressures from McRae's Navier-Stokes code, corresponding with the Reynolds number $R_{L_\infty} = 32 \times 10^6$, are in close agreement with Rainbird's measurements (Refs. 28, 29). Figures 12(a)-12(c) illustrate corresponding qualitative trends in the circumferential pressure distributions at the 0.85 axial station for all Mach numbers tested.

As the three-dimensional boundary layer develops from the windward attachment line region ($\phi = 0°$) toward the minimum pressure point at $\phi \sim 100°$, the crossflow grows rapidly. At Mach 0.6, toward which the bulk of the remaining discussion in this paper will be devoted, Fig. 13 provides a comparison between some preliminary surface shear stress directions (relative to the cone generators), ω, obtained from oil dot streaks and those angles deduced from the bidirectional buried hot-wire gage. The maximum value of ω given from the gage is close to 40° in the vicinity of the minimum pressure point. The boundary layer, in proceeding around the lee side of the cone, now encounters a strong circumferential adverse pressure gradient and thickens rapidly (see Fig. 8). The crossflow angle, ω, reduces progressively to zero, Fig. 13, at which point the shear stress trajectories converge and run parallel to a generator, the primary

---

*We should be aware, however, that in solving the Euler equations of motion for the inviscid flow about a circular cone at incidence in supersonic flow (Refs. 51, 52), we find that nonlinear normal forces begin to develop also at a relative incidence close to 1.5 for this $M_\infty = 1.8$ case. These inviscid components of overall normal force are more than 50% of the total nonlinear force, as we see from the additional symbols plotted on Fig. 6. The effects of viscous growth on the windward circumferential pressure distribution are minor but, as expected, the inviscid lee-side pressures are changed substantially due to the vortices (see Fig. 12(a)).

separation line, ϕ_{s1} (see the schematic drawing in Fig. 4(a)). Discrepancies between the oil flow results and shear stress directions as deduced from the wire voltages await resolution in a forthcoming repeat experiment. The laser flow visualization in Fig. 8 and the contours of local pitot pressure deficit plotted in Fig. 9 illustrate the vortex core position and the close comparison between the boundaries of the free shear layers from these two measurements. The discrepancies in core position between the pitot and vapor screen measurements and the disagreement between ϕ_{s1} positions on Figs. 9 and 13 may be due to a displacement effect caused by the blockage of the pitot array. Beyond the circumferential angle ϕ_{s1}, Fig. 12 indicates there is a plateau of virtually constant pressure (particularly at Mach 1.8) followed by a second pronounced pressure minimum and finally a recovery toward the leeward generator. The second pressure minimum caused by the induced effect of the primary vortices drains fluid from the region of the leeward generator, appreciably thinning the flow there. This movement of fluid beneath the vortices itself separates from the cone surface at ϕ_{s2} on a scale substantially smaller than the primary flow. The lobular region of secondary flow is shown by the pitot contours of Fig. 9, although it is not evident on the vapor screen photograph shown in Fig. 8. Between ϕ_{s1} and ϕ_{s2}, there must be yet another divergent attachment line region where $\omega = 0$ (see Figs. 4(a) and 13) from which fluid diverges to feed both separation lines.

The magnitude of the resultant surface shear stress at the 0.85 axial station in subsonic flow obtained from the yawed buried hot wire pair is shown in Fig. 14. The maximum uncertainty in the absolute levels of shear stress deducible from the wires is about ±15%. Again, the variation of the local skin friction coefficient with circumferential angle at Mach 0.6 follows the trends established in Rainbird's Mach 1.8 and 4.25 measurements (Refs. 28, 29). The skin friction reduces smoothly to a minimum, but finite, value at the primary separation line that is lower than the zero incidence attached flow value. The skin friction is again a minimum at the secondary separation with high values due to the divergent attachment line flows between the separation lines and along the leeward meridian. The boundary layer along the leeward generator, in fact, accelerates rapidly in the lateral sense due to the very favorable pressure gradient caused by the vortices (see Fig. 12(c)). The shear stress increases to a value well above that at the windward generator with a concomitant surface shear direction of -20° at $\phi \sim 170°$.

3.1.3 Fluctuation Measurements

The fluctuating pressure field within a viscous flow is associated with the irregular motions of the turbulence; from the interaction of the turbulent fluctuations normal to the wall with the mean shear, and from the interaction of the turbulence with itself. In incompressible flow, the pressure fluctuations at one station in the flow are produced by momentum fluctuations at many other stations (Poisson's equation). Thus the pressure at one point will not correlate with velocity fluctuations at another point in close proximity (Ref. 56).

Now the pressure fluctuations have a wide range of sizes typically equal in scale to boundary-layer thickness on down to ν/u_τ. But according to Bradshaw (Ref. 57), the spectrum of pressure fluctuations at a wall beneath a two-dimensional turbulent boundary layer as it approaches separation is constituted of essentially high-frequency and low-frequency energy. The high-frequency components are generated in the small-scale inner region (the so-called law of the wall region) whereas the low-frequency pressure fluctuations emanate from the larger-scale outer region. In the latter, the fluctuations intensify as the wake region of the boundary layer increases in thickness. Under two-dimensional attached boundary layers, the level of pressure fluctuation also scales with the mean wall shear stress. In adverse pressure gradients, the pressure fluctuation scales with the outer variables as the law-of-the-wall region now becomes very small. Irrespective of the pressure gradient, however, the absolute level of the wall pressure fluctuations is small, and it is difficult to isolate the fluctuations from turbulence and sound generated by free-stream disturbances in a typical, large wind tunnel. At Mach 0.6, the disturbance level of the NASA 1.8- by 1.8-m tunnel stream is high, and probably consists of fluctuations in vorticity, temperature, and sound. It is thought that the signal at the cone surface is especially contaminated with the radiated sound from the tunnel wall boundary layers and slots in the tunnel ceiling and floor. Figure 15 shows the rms pressure fluctuation at the cone surface beneath the Mach 0.6 axisymmetric boundary layer to be $\langle p' \rangle / q_\infty \sim 0.03$, a value 10 times the level of mean shear stress (see Fig. 14). This is in contrast with a value of 3 times the mean shear stress quoted by Kistler and Chen (Ref. 58) for a two-dimensional, subsonic, attached flow, beneath a reasonably "quiet" free stream. The spectra at zero angle of attack (not shown) exhibited peaks at frequencies of 800 and 1600 Hz. Neither the levels of the peaks nor the areas beneath them appeared dependent on roll orientation or angle of incidence, however, and these peaks were not filtered out in the results to be presented. The interference of the tunnel noise field on the development of the attached boundary layers, may well have a different effect than on the free shear layers. Particular frequencies, if dominant, may excite instabilities in the latter flow. Under these circumstances then, Fig. 15 also shows the rms pressure fluctuations at the 0.85 station for the Mach 0.6 flow at a relative incidence of 2.5. These fluctuating pressures were measured simultaneously with the mean pressures already discussed on Fig. 12(c). We note from Fig. 15 that the absolute level of rms pressure fluctuation (actually plotted relative to the constant dynamic pressure of the free stream) increases in the favorable pressure gradient from the windward attachment line toward the minimum pressure point, then decreases smoothly in the adverse pressure gradient to a minimum value at the primary separation line. The signal increases rapidly again as the leeward attachment line region is approached. Between the positions of primary and secondary separation, ϕ_{s1} and ϕ_{s2}, there is slight evidence that the fluctuation level once more increases at the reattachment line, ϕ_A. These results bear comparison with those beneath two-dimensional separation bubbles (Ref. 59), although the two-dimensional separation is, of course, the special limiting case of the more general swept separation in three dimensions. Mabey (Ref. 59) showed that the pressure fluctuations caused by fluctuations in the two-dimensional separation line position were small, whereas at reattachment, the pressure fluctuations exceeded those at the separation point by 4 to 10 times.

In apparent contradistinction with these results, however, Schloemer (Ref. 60) and Burton (Ref. 61) have reported on pressure fluctuations beneath two-dimensional attached boundary layers in both adverse and favorable pressure gradient conditions, and found what appears to be the converse of the pressure fluctuation behavior on the cone surface. Relative to a zero pressure gradient flow, $\langle p' \rangle / q_\infty$ was greater in the adverse and less in the favorable pressure gradients. The differences were accentuated in the

two-dimensional flow if the normalizing parameter for the rms wall pressures was the wall shear stress. But, it should be noted that if the cone surface rms pressure data are plotted with respect to the resultant wall shear stress, a corresponding accentuation relative to the zero pressure gradient, $\alpha = 0°$ case, is to be seen in Fig. 15.

On the basis of the dimensionless pressure measurement hole parameter, $(d_p u_\tau)/\nu$, which is upward of 300 in our Mach 0.6 experiment, we are probably missing the dramatic increase in intensity of the small-scale pressure fluctuations that Emmerling (Ref. 62) has noted, for example (see Ref. 56). This parameter should be less than 50 if the small-scale fluctuations are to be measured. But it will be shown that the pressure fluctuations are dominated by low-frequency components in the adverse pressure gradient regions so that loss of high-frequency response would not explain the substantial difference between the two-dimensional and the three-dimensional results. Neither would we expect, perhaps, that the grazing shear flow over a surface orifice would produce changes in acoustical impedance of the port (which are dependent on frequency) that were large enough to overturn the trends seen at the cone surface. Willmarth and Yang (Ref. 63) showed that the transverse curvature of the model surface alters the large eddies significantly; but their boundary-layer thickness was of order of model cross-section diameter, whereas on the cone, it is 1/100 of the local cone diameter.

If the rms pressure results are not spurious because of the high background noise level, then the character difference may be attributable to the escape provided to the flow in a three-dimensional separation in contrast with the two-dimensional case.

The behavior of the rms values of output voltage signal (made nondimensional with respect to the flow-based signal strengths) for each of the buried hot-wire pair on the cone surface, peak at the separation lines. Figure 16, for example, presents the normalized fluctuations from one wire to illustrate that these peak levels are more than double those beneath the attached (and reattached) flow regions. The second wire provided essentially the same normalized output so that the normalization virtually removes the sensitivity to yaw.

If conduction losses are negligible from the wire to the substrate, and if the wire is normal to the local shear stress direction, we may see from Eq. (1) that the mean square of the voltage fluctuation at the wire is related to the pressure and shear stress fluctuations

$$\overline{\left(\frac{e'}{E}\right)^2} \sim \left[\overline{\left(\frac{p'}{p_w}\right)^2} + 2\overline{\left(\frac{p'\tau'}{p_w\tau_w}\right)} + \overline{\left(\frac{\tau'}{\tau_w}\right)^2}\right]$$

The order of the present results implies that at separation, if $\langle p'\rangle/p_w$ is a minimum (see Fig. 15) and $\langle e'\rangle/E$ is a maximum, then $\langle\tau'\rangle/\tau_w$ must be large for the equality to be valid, irrespective of the correlation between p' and τ'. Along a line of divergence of limiting streamlines, $\langle p'\rangle/p_w$ is large, $\langle e'\rangle/E$ is small, and hence $\langle\tau'\rangle/\tau_w$ must be equal to the order of the pressure fluctuation with a negative correlation. In other words, the shear stress fluctuations are large both at the separation lines and along the attachment line regions corresponding to large gradients of fluctuating velocity. Let us now look at the correlations between values of the fluctuating voltage at different instants of time for the same hot wire that was shown in Fig. 16; for how the correlation coefficient decreases with increasing time depends on the character of the turbulence. Seven such autocorrelations are presented in Fig. 17, corresponding to circumferential positions on the cone surface between $90° < \phi < 180°$. The correlation functions all decrease toward zero, more-or-less monotonically, falling faster initially from unity in the favorable pressure gradient three-dimensional boundary layer (e.g., at $\phi = 90°$) than in the retarded flow ($\phi = 135°$, $140°$). This corresponds with a preponderance of energy at higher frequencies in the attached flow and at lower frequencies in the retarded flow. At the separation lines, these large-scale motions give rise to the rms overshoots from the buried hot wire observed on Fig. 16, and the overshoots in pressure fluctuation normalized by the mean shear stress on Fig. 15. The correlation curves demonstrate the substantial changes in lee-side flow toward and subsequent to primary separation. A normalized time scale in terms of outer flow variables such as $(t_p u_\infty)/\delta^*$ is not used because the boundary-layer displacement thickness is unknown.

We may deduce some important notions concerning the eddy structure in the flow from the curvature of the correlation curves (Ref. 64). All component eddies are roughly of the same size when the curvature is not especially large anywhere. Such behavior is noted in the adverse pressure gradient flow ($\phi = 135°$, $140°$, and up to $\phi = 145°$) where large eddies dominate. (An approximate measure of the "longest connection in turbulent behavior" (Ref. 65) may be gained from the area beneath the correlation curve, and ϕ_{s1} provides the largest area.) The same characteristic is also shown in the very thin boundary layer along the leeward meridian where small eddies must be the overwhelming constituents. A wide range of eddy sizes, on the other hand, is indicated by local regions of high curvature in the correlation curves. This may occur near the origin, but cannot be ascertained categorically. Alternatively, when there are two distinct ranges of eddy size present, the correlation curve appears as a summation of two correlation functions of substantially different scales. We note this characteristic, in particular, for the boundary layer having reacted to the favorable pressure gradient ($\phi = 90°$), then a diminution of this property through the primary separation region to begin again at the reattachment line, $\phi_A = 155°$. The two ranges of eddy size would also appear to exist at the secondary separation line, $\phi_{s2} = 160°$, from which a coiled vortex does not appear to have developed yet (see Fig. 9).

The autocorrelation is related approximately to the spectral density by a Fourier transform. Spectra are shown in Fig. 18 corresponding to most of the autocorrelations displayed in Fig. 17. The ordinates are in the ratio of the mean square values of voltage fluctuation at each circumferential station divided by the value at primary separation. In conjunction with previous observations, as the three-dimensional boundary layer thickens progressively toward ϕ_{s1}, the energy associated with the large eddies spreads to lower frequencies (as is the case at ϕ_{s2} also). The converse is noted along the leeward meridian. When two distinct ranges of eddy size exist, the spectrum functions should also take a noticeable two-component form similar to those of the correlation functions, as we see at $\phi_A = 155°$ and $\phi_{s2} = 160°$.

Having witnessed these substantial changes, it would appear that, in calculating complex, three-dimensional viscous flows leading to separation, the use of turbulence models that do not recognize the large changes in spectra in at least a qualitative way will not be representative of the physics of the flow.

3.2 Lee-Side Flow About a Tangent-Ogive/Cylinder

3.2.1 Mean Flow Field

As mentioned previously, some supportive three-dimensional laser velocimeter measurements of mean and fluctuating velocity about a slender tangent ogive/cylinder (Fig. 19) were obtained by Owen and Johnson (Ref. 49) at a relative incidence of 2.3. The measurements were made in the Ames 0.6- by 0.6-m (2- by 2-ft) Transonic Wind Tunnel at a Mach number of 0.6 and Reynolds number based on the 0.3-m (1-ft) total length of the body, equal to $R_{L_\infty} = 2 \times 10^6$. The velocity field in the wake was measured with a two-color forward scatter frequency-offset laser velocimeter, allowing two velocity components perpendicular to the axis to be obtained simultaneously. Since we are seeking three velocity components, however, two sets of measurements must be taken. In the first set, the laser beams were normal to the tunnel axis so that the axial (u) and vertical (w) velocity components were found. From these two components could be obtained the vertical velocity in the crossflow plane perpendicular to the body axis (see Fig. 19). For the second set, the transmitting optics were rotated 30° about the z-axis and measurements taken again. Now, one velocity component measured was again the vertical velocity whereas the second was a combination of the axial velocity (u) and the lateral velocity (v) in wind-tunnel coordinates. Thus, since the axial velocity had already been measured, the lateral velocity could be calculated. In other words, the lateral velocity in the crossflow plane is obtained, since it is the same in both wind-tunnel and body coordinates.

Bragg cells, which produced zero-velocity frequency offsets in both color systems, were incorporated to remove directional ambiguity from the measurements. Without this capability, Owen and Johnson (Ref. 49) have cautioned against believing any measurements in flows that are unsteady or possess a high degree of turbulence. Since with increasing Mach number the helix angle of a streamtube becomes smaller with respect to the axis of the vortex, larger axial distances are required for particles to reach the core regions. Thus an artificial aerosol was introduced into the wind-tunnel flow to provide adequate intensity of the scattered light with a count mean diameter of 0.7 micron. Additional details of the instrumentation are given in Ref. 49.

Figure 20 shows the crossflow velocity vector field at 4 diameters from the nose, just aft of the ogive/cylinder junction where we detect that the vortex core positions are located along $\tilde{z}/d \sim 0.9$ at $y/d \sim 0.3$. Note the slight asymmetry, but the resemblance to the cone lee-side flow. The vertical velocities, $\tilde{w}$, in the crossflow plane are plotted in Fig. 21, the maximum down-flow values ($\sim u_\infty$) occurring in the pitch plane of symmetry as the leeward meridian is approached. This large down-flow is a relatively narrow region between the rotational pair and is highlighted as an intense line of maximum vapor concentration in the cone crossflow visualization displayed in Fig. 8 (and see later, Fig. 26). The velocity gradient through the core region at $\tilde{z}/d \sim 0.9$ is virtually infinite on the scale of measurement resolution as it is on the axial velocity distributions displayed in Fig. 22. At the stations approaching the leeward meridian where the crossflow is largest, the axial velocity is lowest. The axial velocity then increases very rapidly across the vortex to a value overshooting the free-stream by about 20%.

Lateral crossflow velocities ($\tilde{v}$) resolved from the measurements normal to and 30° to the tunnel axis are shown in Fig. 23. As expected, a pass through the core positions at $\tilde{z}/d = 0.9$ shows virtually zero velocity. Moving to traverses above and below the vortex centers shows the lateral velocities to be at maximum levels at y/d values in line with the cores.

3.2.2 Fluctuating Velocities

Some insight into the turbulent and unsteady nature of the vortex flow field about the ogive-cylinder has also been obtained with the laser velocimeter. These data in Figs. 24 and 25, obtained at $\tilde{z}/d = 0.9$ through the vortex cores, show peaks in the rms velocity, one on each side of the pitch-plane close to the regions of maximum mean velocity gradient (the core centers?). In addition, the rms fluctuation levels remain substantial in regions of small and zero mean velocity gradient, suggesting that large scale turbulence is present throughout the lee-side domain.

3.3 Asymmetrical Separation of the Lee-Side Cone Flow

Figure 26 is a laser-vapor screen crossflow picture of the Mach 0.6 lee-side separated flow about the cone once asymmetry has commenced at a relative incidence just less than 3. As the symmetry developed, the vortices began "bumping together" with increasing unsteadiness to cause large values of rms side force even when the mean side force was near zero. At this particular combination of Mach number, Reynolds number, and configuration of 4% nose bluntness, the starboard vortex moved away from the surface and the port vortex remained more-or-less stationary. As incidence increased to higher values, the unsteady interaction between the vortices increased in intensity and the starboard vortex moved even farther from the surface and rolled over the port side rotational flow. In so doing, the entire lee-side flow indicated diffusion of the well-organized helical vortex structures but there was no visual evidence of periodic shedding.

Along with this movement of the lee-side flow, we would expect the resultant force vector to move towards the side of the cone to which one vortex is closest. This is seen in Fig. 27, where in the subsonic/transonic Mach number range $0.6 < M_\infty < 0.95$ (at $R_{L_\infty} = 13.5 \times 10^6$), the initial direction of side-force development remains the same. As Mach number increases to supersonic speeds, the start of the side force is less precise. Therefore, the critical angles of incidence for onset of side-force development are plotted in Fig. 28 as where the mean side force has reached 5% of the normal force. We detect that depending on the nose bluntness, free-stream Mach number, Reynolds number (and, no doubt, the unknown free-stream fluctuation level), the onset angle of incidence varies between 2.5 and 4.5 times the cone seminose angle. This range is somewhat higher than the nominal values of 2 reported for sharp forebodies by Keener and

Chapman (Ref. 6) at Mach numbers less than 0.6. It is clear that operating with a sharp apex causes an earlier onset of side force as does the very high Reynolds number of 35×10^6. Up to Mach 1, on the other hand, whereas the same observation can be made for the 13.5×10^6 relative to the 4.5×10^6 tests, the reverse is true in supersonic flow.

The effect of rolling the cone in 90° increments and then pitching through the α range is illustrated in Fig. 29 at a constant length Reynolds number of 13.5×10^6. For roll angles 180° apart, the side-force development is in opposite directions as we might suppose if it were a small geometrical imperfection at the nose systematically perturbing the flow development. Figure 29 shows also that lowering the Reynolds number from 13.5×10^6 (essentially turbulent) to 4.5×10^6 (perhaps transitional) delays the onset of side force and shows that repeatability at a given test condition is good.

We await laser velocimeter measurements in the crossflow to report on the fluctuations in the lee-side flow as asymmetry develops.

4. CONCLUSIONS

Based on relatively high Reynolds number measurements of mean and fluctuating flow quantities on the surface of a yawed 5° semiangle circular cone at a Mach number of 0.6 in association with overall force, laser-vapor screen, and mean surface pressure measurements in the expanded Mach number range $0.6 < M_\infty < 1.8$, we conclude that:

1. The development of the viscous flow and separation about this cone at low Mach numbers follows closely the diagnosis of Rainbird (Refs. 28, 29) at higher Mach numbers. As the relative incidence increases, there is a progressive quasi-steady development of symmetrically disposed lobes of vortical fluid that eventually form tightly coiled vortices close to the leeward plane of symmetry. Secondary separations from the surface are found beneath the primary vortices with further increase of incidence. When the relative incidence exceeds about 2.5, the lee-side flow becomes increasingly unsteady and antisymmetrical with respect to the pitching plane causing substantial side forces to develop of magnitude near the values of normal force.

2. In subsonic flow, the fluctuation voltage levels from buried wires in the cone surface, provided evidence of an increase in turbulent eddy size as the primary separation line was approached, and a decrease of eddy size in the thin boundary-layer leeward attachment line region. At the separation lines, these large-scale motions give rise to overshoots in rms fluctuating voltage levels from the buried wires in the surface, and overshoots in rms pressure fluctuations when normalized by the mean-shear stress. Notwithstanding, the absolute level of rms pressure fluctuation decreased in the circumferential adverse pressure gradient to a minimum at the positions of the conical separation lines, and increased to a maximum at the leeward attachment line. This behavior is contrary to that found beneath two-dimensional attached boundary layers in adverse and favorable pressure gradients by other experimenters.

3. The resultant mean-shear stress was always finite, being lower at the separation line positions and higher at the attachment lines.

REFERENCES

1. Peake, D. J.: Phenomenological Aspects of Quasi-Stationary Controlled and Uncontrolled Three-Dimensional Flow Separations. Three-Dimensional and Unsteady Separation at High Reynolds Numbers, AGARD-LS-94, Feb. 1978.

2. Küchemann, D.: Report on the IUTAM Symposium on Concentrated Vortex Motions in Fluids. Jour. Fluid Mechanics, part 1, vol. 21, 1965, pp. 1-20.

3. Maskell, E. C.; and Küchemann, D.: Controlled Separation in Aerodynamic Design. RAE TM 463, Mar. 1955.

4. Rainbird, W. J.; Crabbe, R. S.; Peake, D. J.; and Meyer, R. F.: Some Examples of Separation in Three-Dimensional Flows. CASI Journal, vol. 12, no. 10, Dec. 1966, pp. 409-423.

5. Peake, D. J.; Rainbird, W. J.; and Atraghji, E. G.: Three-Dimensional Flow Separations on Aircraft and Missiles. AIAA Journal, vol. 10, no. 5, May 1972, pp. 567-580.

6. Keener, E. R. and Chapman, G. T.: Onset of Aerodynamic Side Forces at Zero Sideslip on Symmetric Forebodies at High Angles of Attack. AIAA Paper 74-770, Aug. 1974.

7. Keener, E. R.; Chapman, G. T.; Kruse, R. L.: Effects of Mach Number and Afterbody Length on Onset of Asymmetric Forces on Bodies at Zero Sideslip and High Angles of Attack. AIAA Paper 76-66, Jan. 1976.

8. Tobak, M.: On Local Inflexional Instability in Boundary-Layer Flows. Journal of Applied Mathematics and Physics (ZAMP), vol. 24, 1973, pp. 330-354.

9. Rao, D. M.: Side-Force Alleviation on Slender, Pointed Forebodies at High Angles of Attack. AIAA 78-1339, Aug. 1978.

10. Keener, E. R.; and Chapman, G. T.: Similarity in Vortex Asymmetries over Slender Bodies and Wings. AIAA Journal, vol. 15, no. 9, September 1977, pp. 1370-1372.

11. Shanks, R. E.: Low-Subsonic Measurements of Static and Dynamic Stability Derivatives of Six Flat-Plate Wings having Leading-Edge Sweep Angles of 70° to 84°. NASA TN D-1822, 1963.

12. Nielsen, J. N.: Non-Linearities in Missile Aerodynamics. AIAA Paper 78-20, Jan. 1978.

13. Allen, H. J.; and Perkins, E. W.: Characteristics of Flow over Inclined Bodies of Revolution. NACA RM A50L07, Mar. 1951.

14. Küchemann, D.; and Weber, J.: Vortex Motions. Zamm 45, 1965, pp. 457-474.

15. Lamont, P. J.; and Hunt, B. L.: Prediction of Aerodynamic Out-of-Plane Forces on Ogive-Nosed Circular Cylinders. Journal Spacecraft and Rockets, vol. 14, no. 1, Jan. 1977, pp. 38-44.

16. Deffenbaugh, F. D.; and Koerner, W. G.: Asymmetric Vortex Wake Development on Missiles at High Angles of Attack. Journal Spacecraft and Rockets, vol. 14, no. 3, Mar. 1977, pp. 155-162.

17. Maskell, E. C.: Flow Separation in Three Dimensions. RAE Aero. Report 2565, Nov. 1955.

18. Brown, S.: Singularities Associated with Separating Boundary Layers. Royal Society of London Phil. Trans., Series A, vol. 257, 1965, pp. 409-444.

19. Legendre, R.: "Séparation de L'Écoulement Laminaire Tridimensionnel," La Recherche Aéronautique, No. 54, pp. 3-8, Nov.-Dec. 1956.

20. Lighthill, M. J.: Attachment and Separation in Three-Dimensional Flow. Laminar Boundary Layers, Sect. II.2.6, L. Rosenhead, ed., Oxford University Press, 1963, pp. 72-82.

21. Crabbe, R. S.: Flow Separation about Elliptic Cones at Incidence. NAE Aero. Report LR-436, National Research Council of Canada, Aug. 1965.

22. McRae, D. S.: The Conically Symmetric Navier-Stokes Equations: Numerical Solution for Hypersonic Cone Flow at High Angle of Attack. AFFDL-TR-76-139, Mar. 1977.

23. McRae, D. S.; and Hussaini, M. Y.: Supersonic Viscous Flow over Cones at Incidence. Sixth International Conference on Numerical Methods in Fluid Dynamics, Tbilisi, USSR, June 1978.

24. Rakich, J. V.; and Lubard, S. C.: Numerical Computation of Viscous Flows on the Lee Side of Blunt Shapes Flying at Supersonic Speeds. NASA SP-347, Mar. 1975, pp. 531-542.

25. Smith, J. H. B.: Inviscid Fluid Models, Based on Rolled-up Vortex Sheets, for Three-Dimensional Separation at High Reynolds Number. Three-Dimensional and Unsteady Separation at High Reynolds Numbers, AGARD-LS-94, Feb. 1978.

26. MacCormack, R. W.: The Effect of Viscosity in Hypervelocity Impact Cratering. AIAA Paper 69-354, 1969.

27. Tracy, R. R.: Hypersonic Flow over a Yawed Circular Cone. GALCIT Memo No. 69, Grad. Aero. Labs., California Institute of Technology, Pasadena, California, 1963.

28. Rainbird, W. J.: The External Flow Field about Yawed Circular Cones. AGARD CP-30, May 1968.

29. Rainbird, W. J.: Turbulent Boundary-Layer Growth and Separation on a Yawed Cone. AIAA Journal, vol. 6, no. 12, Dec. 1968.

30. Cleary, J. W.: Effects of Angle of Attack and Bluntness on Laminar Heating Rate Distribution on a 15° Cone at Mach Number of 10.6. NASA TN D-5450, Oct. 1969.

31. Agarwal, R.: Private communication, July 1978.

32. Pulliam, T. H.; and Steger, J. L.: On Implicit Finite-Difference Simulations of Three-Dimensional Flow. AIAA Paper 78-10, Jan. 1978.

33. Smith, J. H. B.: A Review of Separation in Steady, Three-Dimensional Flow. In Flow Separation, AGARD CP-168, May 1975.

34. Rainbird, W. J.; Crabbe, R. S.; and Jurewicz, L. S.: A Water Tunnel Investigation of the Flow Separation about Circular Cones at Incidence. National Research Council of Canada, Aero. Rept. LR-385, Sept. 1963.

35. Guffroy, D.; Roux, B.; Marcillot, J.; Brun, R.; and Valensi, J.: Étude Théorique et Expérimentale de la Couche Limite Autour d'un Cône Circulaire Placé en Incidence dans un Courant Hypersonique. AGARD CP 30, May 1968.

36. Stetson, K. F.: Experimental Results of Laminar Boundary-Layer Separation on a Slender Cone at Angle of Attack at $M_\infty = 14.2$. ARL 71-0127, Aug. 1971.

37. Nebbeling, C.; and Bannink, W. J.: Experimental Investigation of the Supersonic Flow Field about a Slender Cone at High Incidences. Delft University of Technology, Dept. of Aerospace Eng. Rept. LR-233, Nov. 1976.

38. McElderry, E. D.: An Experimental Study of Sharp and Blunt 6-Degree Cones at Large Incidence with a Turbulent Boundary Layer at Mach 6. AFFDL-TM-74-170, Sept. 1974.

39. Mangler, K. W.; and Smith, J. H. B.: A Theory of the Flow Past a Slender Delta Wing with Leading-Edge Separation. Proc. Roy. Soc., Series A, No. 1265, May 1959, pp. 200-217.

40. Smith, J. H. B.: Improved Calculations of Leading-Edge Separation from Slender Delta Wings. Proc. Roy. Soc., Series A, vol. 306, 1968, pp. 67-90.

41. Nebbeling, C.; and Bannink, W. J.: Experimental Investigation of Supersonic Flow Past a Slender Cone at High Incidence. Journal of Fluid Mechanics, vol. 87, part 3, Aug. 1978, pp. 475-496.

42. Whitfield, J. D.; and Dougherty, N. S.: A Survey of Transition Research at AEDC. In Laminar-Turbulent Transition, AGARD CP-224, May 1977.

43. Hanly, R. D.: Effects of Transducer Flushness on Fluctuating Surface Pressure Measurements. Progress in Astronautics and Aeronautics, vol. 46, 1976, pp. 291-302.

44. Higuchi, H.; and Peake, D. J.: A Bi-Directional, Buried-Wire Skin Friction Gage. NASA TM-78531, 1978.

45. Murthy. V. S.; and Rose, W. C.: Wall Shear Stress Measurements in a Shock-Wave Boundary-Layer Interaction. AIAA Journal, vol. 16, no. 7, July 1978, pp. 667-672.

46. Rubesin, M. W.; Okuno, A. F.; Mateer, G. G.; and Brosh, A.: A Hot Wire Surface Gage for Skin Friction and Separation Detection Measurements. NASA TM X-62,465, July 1975.

47. Bradshaw, P.; and Unsworth, K.: A Note on Preston Tube Calibrations in Compressible Flow. Imperial College Aero. Report 73-07, Sept. 1973.

48. McCroskey, W. J.; and Durbin, E. J.: Flow Angle and Shear Stress Measurements Using Heated Films and Wires. ASME Journal Basic Engineering, 94D, pp. 46-52, Mar. 1972.

49. Owen, F. K.; and Johnson, D. A.: Wake Vortex Measurements of Bodies at High Angle of Attack. AIAA Paper 78-23, Jan. 1978.

50. Sims, J. L.: Tables for Supersonic Flow Around Right Circular Cones at Small Angle of Attack. NASA SP-3007, 1964.

51. Schiff, L. B.: A Study of the Nonlinear Aerodynamics of Bodies in Nonplanar Motion. NASA TR R-421, Jan. 1974.

52. Chaussee, D. S.; Kutler, P.; and Holtz, T.: Inviscid Supersonic/Hypersonic Body Flowfield and Aerodynamics from Shock-Capturing Technique Calculations. Journal Spacecraft and Rockets, vol. 13, no. 6, June 1976, pp. 325-331.

53. Ericsson, L. E.: Dynamic Support Interference. Journal Spacecraft and Rockets, vol. 9, no. 7, July 1972, pp. 547-553.

54. Rainbird, W. J.: Errors in Measurement of Mean Static Pressure of a Moving Fluid Due to Pressure Holes. DME/NAE Quarterly Bulletin, No. 1967(3), National Research Council of Canada, Oct. 1967.

55. Franklin, R. E.; and Wallace, J. M.: Absolute Measurements of Static-Hole Error Using Flush Transducers. Journal of Fluid Mechanics, vol. 42, part 1, 1970, pp. 33-48.

56. Willmarth, W. W.: Pressure Fluctuations Beneath Turbulent Boundary Layers. Annual Review of Fluid Mechanics, vol. 7, 1975, pp. 13-38.

57. Bradshaw, P.: Inactive Motion and Pressure Fluctuations in Turbulent Boundary Layers. NPL Aero. Report 1172, Oct. 1965.

58. Kistler, A. C.; and Chen, W. S.: The Fluctuating Pressure Field in a Supersonic Turbulent Boundary Layer. Journal of Fluid Mechanics, vol. 16, part 1, 1963, pp. 41-64.

59. Mabey, D. G.: Analysis and Correlation of Data on Pressure Fluctuations in Separated Flow. Journal of Aircraft, vol. 9, no. 9, Sept. 1972, pp. 642-645.

60. Schloemer, H. H.: Effects of Pressure Gradients on Turbulent Boundary-Layer Wall Pressure Fluctuations. U.S. Navy Underwater Sound Lab. Report No. 747, 1966.

61. Burton, T. E.: Wall Pressure Fluctuations at Smooth and Rough Surfaces under Turbulent Boundary Layers with Favorable and Adverse Pressure Gradients. Acoustics and Vibration Lab. MIT Report No. 70208-9, 1973.

62. Emmerling, R.: The Instantaneous Structure of the Wall Pressure Under a Turbulent Boundary Layer Flow. Max-Planck-Institut für Strömungsforschung Rep. No. 9/1973.

63. Willmarth, W. W.; and Yang, C. S.: Wall Pressure Fluctuations Beneath Turbulent Boundary Layers on a Flat Plate and a Cylinder. Journal of Fluid Mechanics, vol. 41, 1970, p. 47.

64. Townsend, A. A.: The Structure of Turbulent Shear Flow. Cambridge University Press, 1976.

65. Hinze, J. O.: Turbulence. McGraw Hill, 1959, pp. 34-42.

ACKNOWLEDGMENTS

The authors express their gratitude to L. H. Ohman, of NAE Ottawa, for kindly making available to NASA the basic 5° cone model and pitot rake. They also wish to acknowledge the substantial efforts of F. Lemos of Ames Research Center, who fabricated the hot-wire gages and who, along with S. J. Lockyear from NAE (on NASA support) assembled and fitted the intricate instrumentation in the model.

Special thanks are also due to: D. Pena of ARO Inc. for his fine services as project engineer in charge of the tunnel test; to L. J. Rainbird, for conveying previously unpublished side-force results obtained on the same model in the NAE 1.5- by 1.5-m (5- by 5-ft) blowdown wind tunnel; and to D. Chaussee of Nielsen Engineering and Research, for running the inviscid flow code of Ref. 52.

One of us, F. Kevin Owen, would also like to acknowledge the support of the Air Force Armament Laboratory, Eglin, AFB, Florida, and Ames Research Center, Moffett Field, California, under Contract No. NAS2-9663.

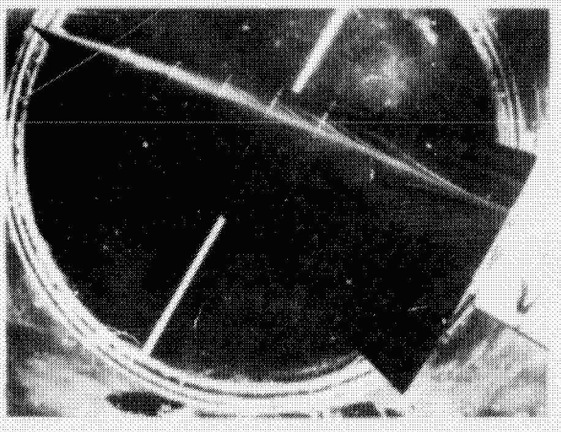

Fig. 1. Limiting Streamlines on 1-1/2:1 Elliptic Cone at 30° Incidence in a Water Tunnel; Laminar; $R_{L_\infty} = 2.7 \times 10^6$ (Crabbe (Ref. 21)).

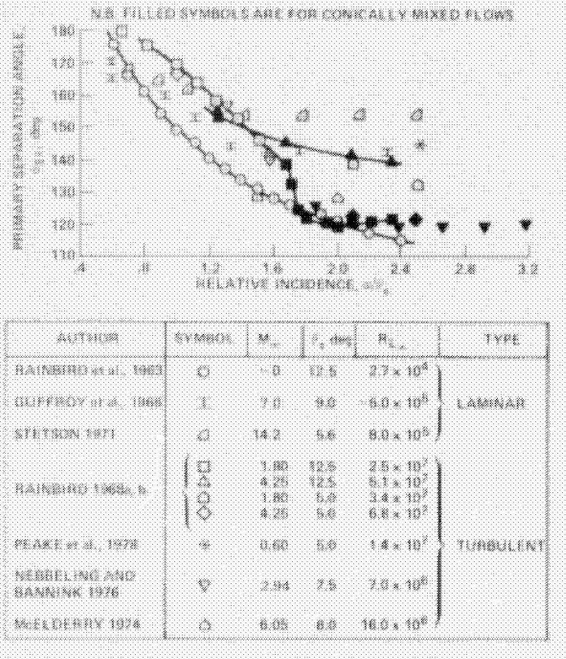

AUTHOR	SYMBOL	M_∞	β, deg	R_{L_∞}	TYPE
RAINBIRD et al., 1963	○	~0	12.5	2.7×10^6	LAMINAR
GUFFROY et al., 1966	△	7.0	9.0	6.0×10^5	
STETSON 1971	□	14.2	5.6	8.0×10^5	
RAINBIRD 1968a, b	□	1.80	12.5	2.5×10^7	TURBULENT
	△	4.25	12.5	5.1×10^7	
	○	1.80	5.0	3.4×10^7	
	◇	4.25	5.0	6.8×10^7	
PEAKE et al., 1978	✳	0.60	5.0	1.4×10^7	
NEBBELING AND BANNINK 1976	▽	2.94	7.5	7.0×10^6	
McELDERRY 1974	⌂	6.05	8.0	16.0×10^6	

Fig. 2. Circumferential Primary Separation Angles on Circular Cones at Incidence (or Yaw).

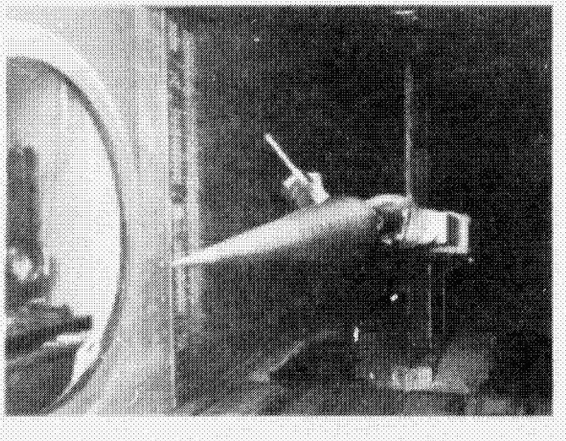

Fig. 3. 5° Cone in NASA Ames 1.8- by 1.8-m (6- by 6-ft) Wind Tunnel.

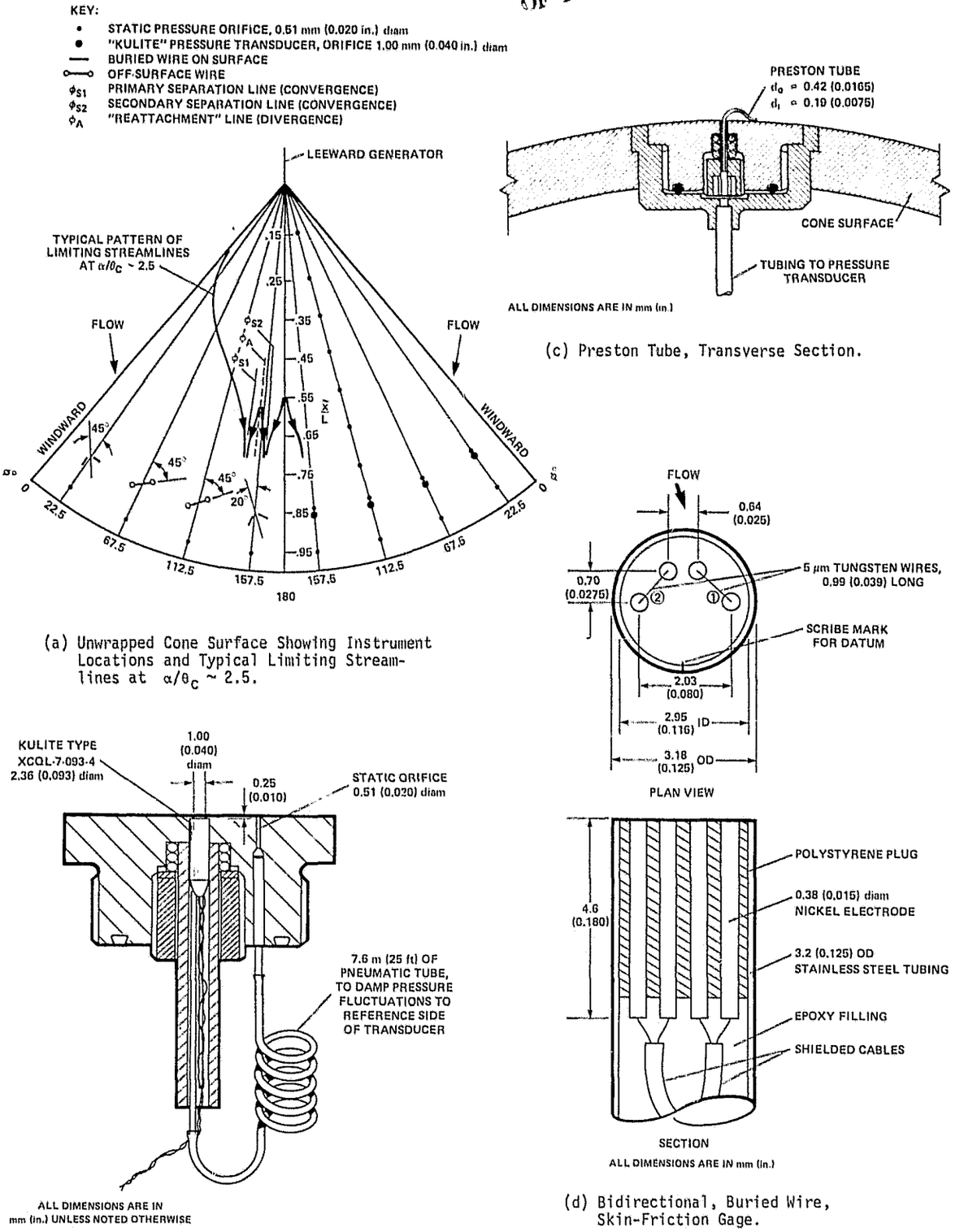

(a) Unwrapped Cone Surface Showing Instrument Locations and Typical Limiting Streamlines at $\alpha/\theta_C \sim 2.5$.

(b) "Kulite" Pressure Transducer, Section Along Cone Generator.

(c) Preston Tube, Transverse Section.

(d) Bidirectional, Buried Wire, Skin-Friction Gage.

Fig. 4. Instrumentation on Cone Surface.

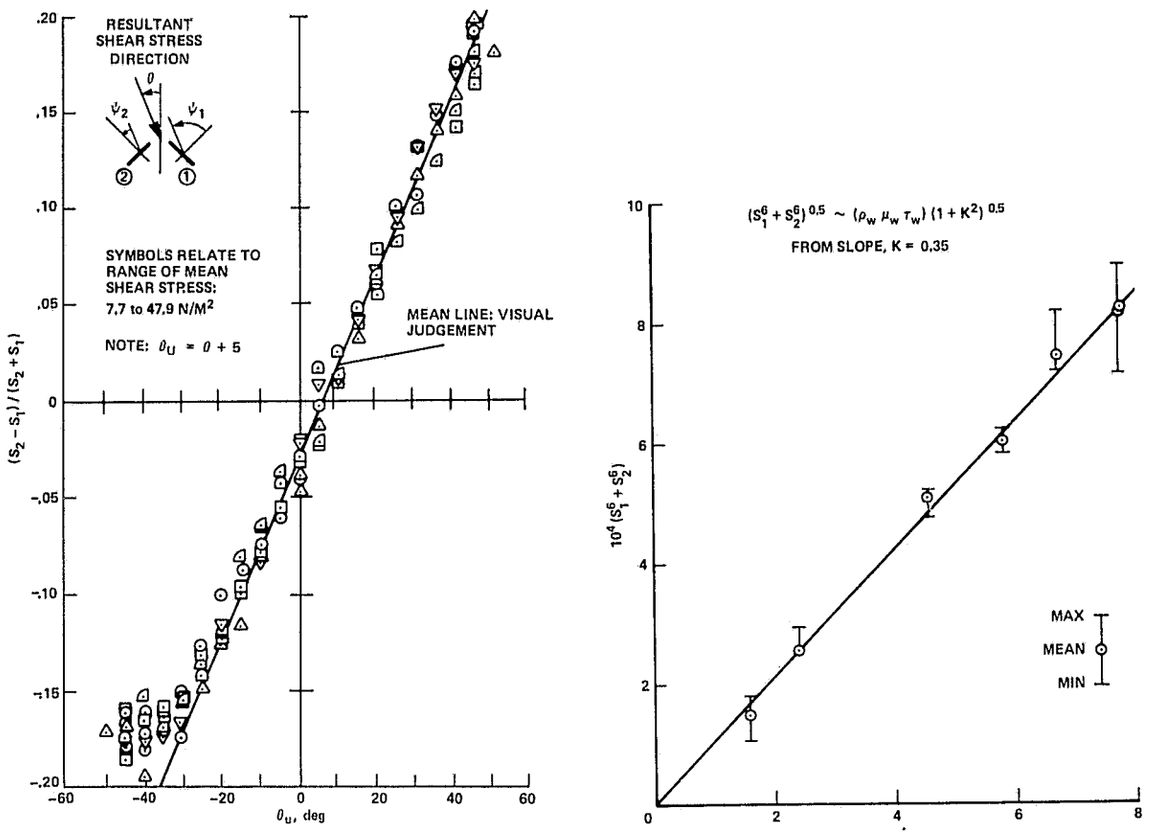

(a) Directional.

(b) Magnitude of Skin Friction.

Fig. 5. Calibrations of Bidirectional, Buried Wire Skin-Friction Gage.

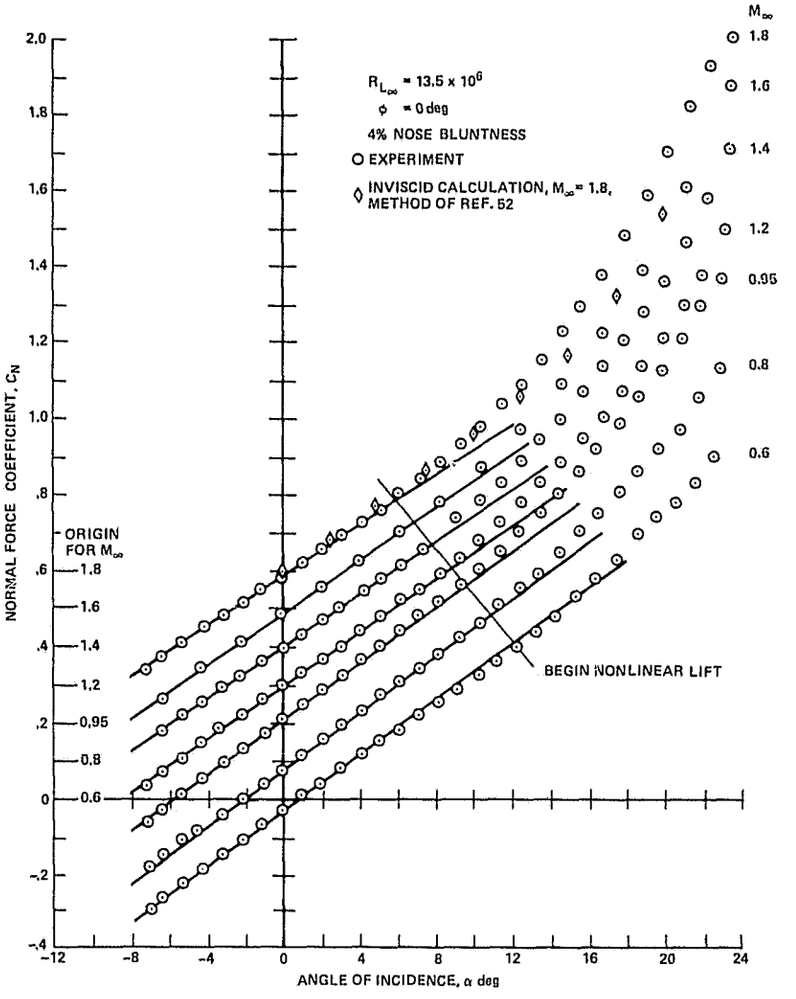

Fig. 6. Normal Forces on 5° Cone for $0.6 < M_\infty < 1.8$.

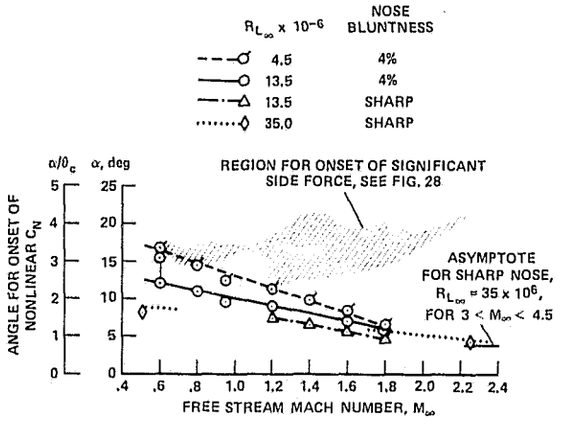

Fig. 7. Onset Boundaries of Nonlinear Normal Force for 5° Cone.

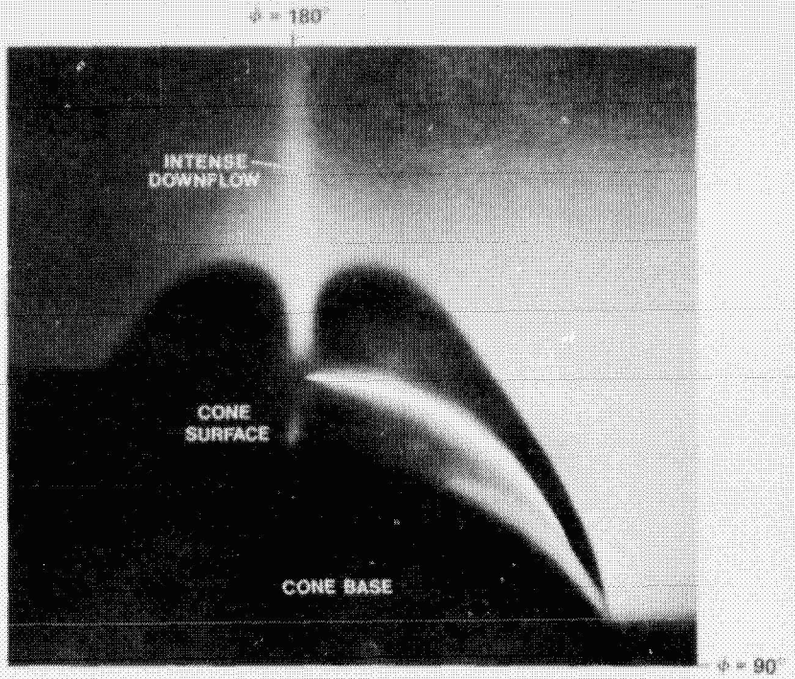

VIEW LOOKING UPSTREAM FROM CONE BASE, AT AXIAL STATION, 0.85 L, WHERE $h_{CORE} \sim 0.16$

Fig. 8. Laser Vapor Screen of Symmetrical Lee-Side Flow Separation on 5° Cone at $\alpha/\theta_c \sim 2.5$, $M_\infty = 0.6$, $R_{L_\infty} = 13.5 \times 10^6$.

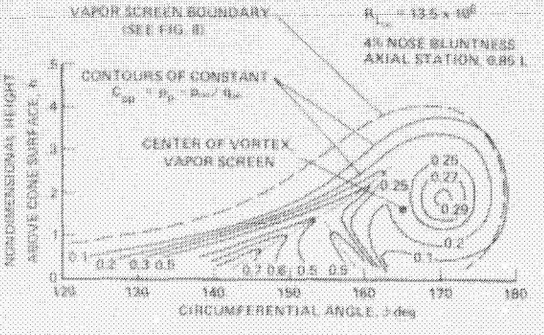

Fig. 9. Contours of Pitot Pressure Deficit in Symmetrical Lee-Side Flow Separation at $\alpha/\theta_c \sim 2.5$, $M_\infty = 0.6$.

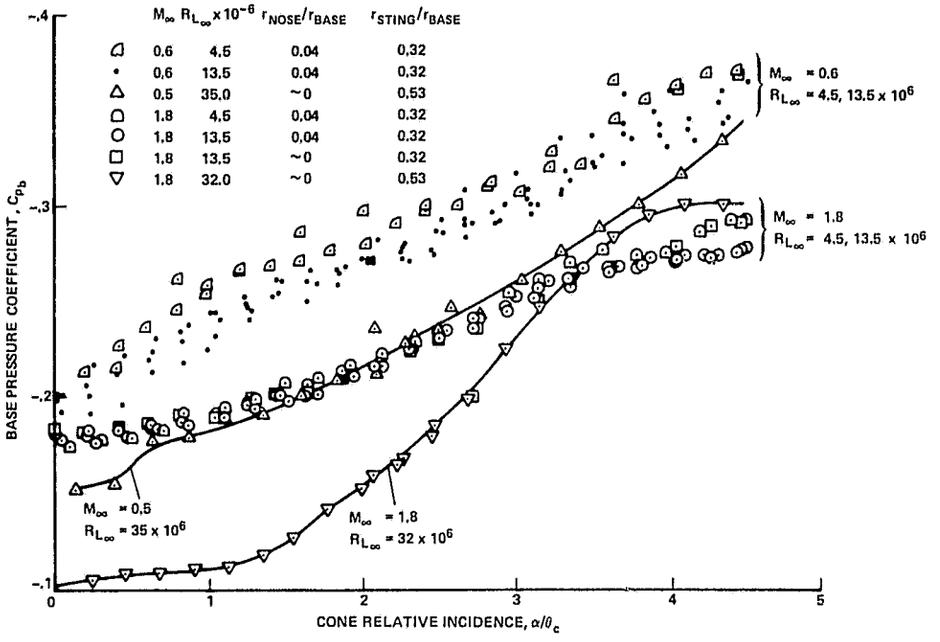

Fig. 10. Base Pressures on 5° Cone.

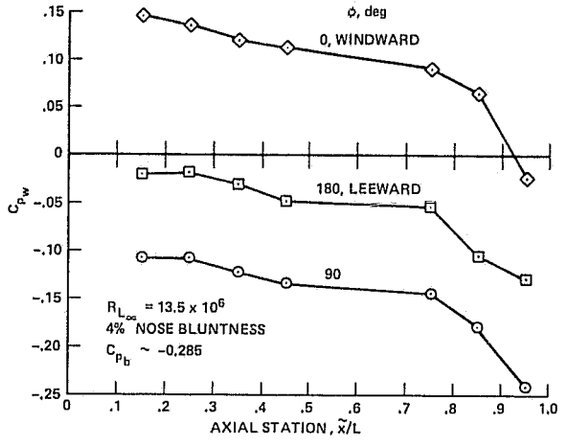

Fig. 11. Base Effect on Pressure Along Cone Generators at $\alpha/\theta_c \sim 2.5$, $M_\infty = 0.6$.

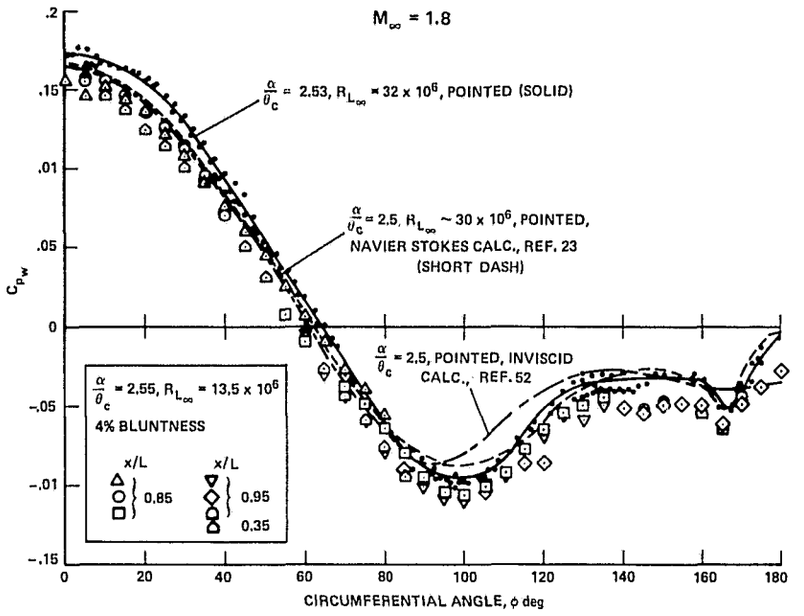

(a) M_∞ 1.8.

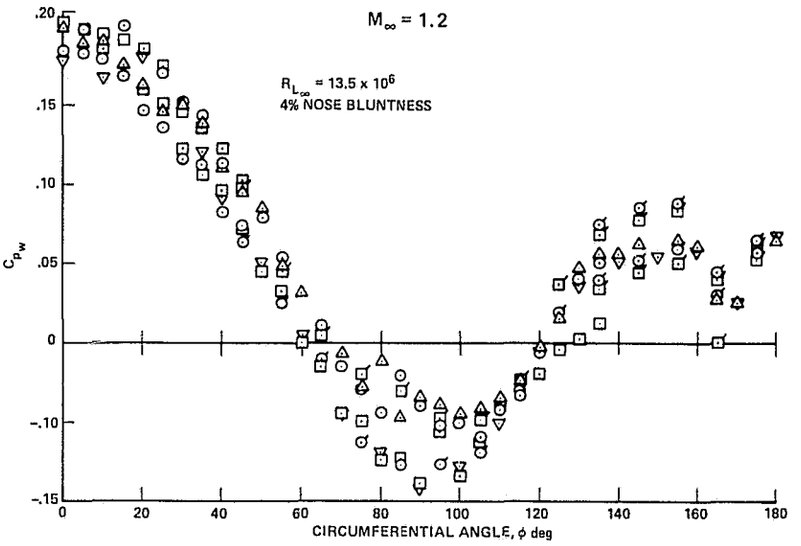

(b) M_∞ = 1.2.

Fig. 12. Circumferential Distributions of Mean Static Pressure on 5° Cone at α/θ_c ~ 2.5.

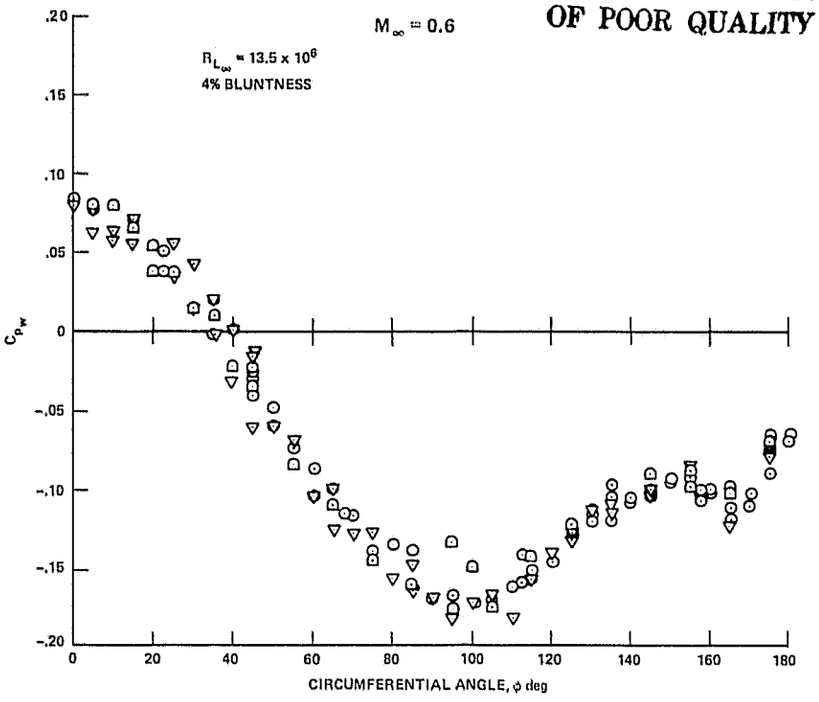

(c) M_∞ = 0.6.

Fig. 12. Concluded.

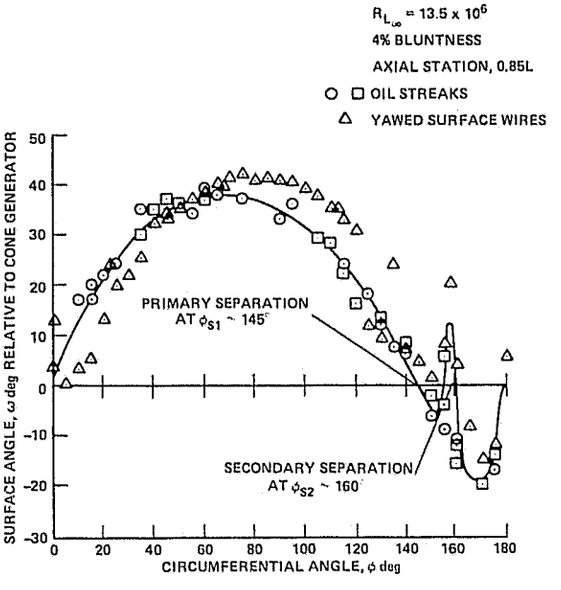

Fig. 13. Surface Shear Stress Directions Around 5° Cone at $\alpha/\theta_c \sim 2.5$, $M_\infty = 0.6$.

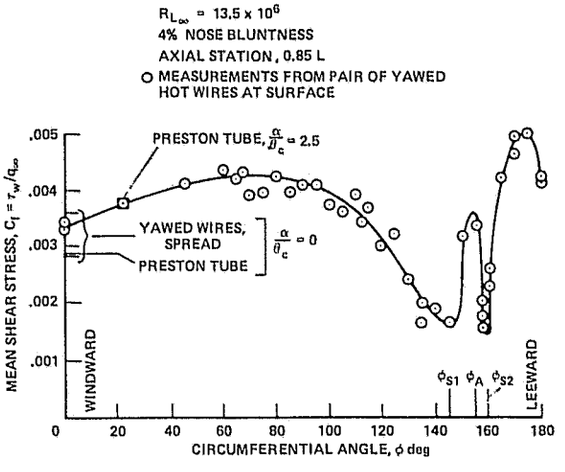

Fig. 14. Skin Friction Around 5° Cone at $\alpha/\theta_c \sim 2.5$, $M_\infty = 0.6$.

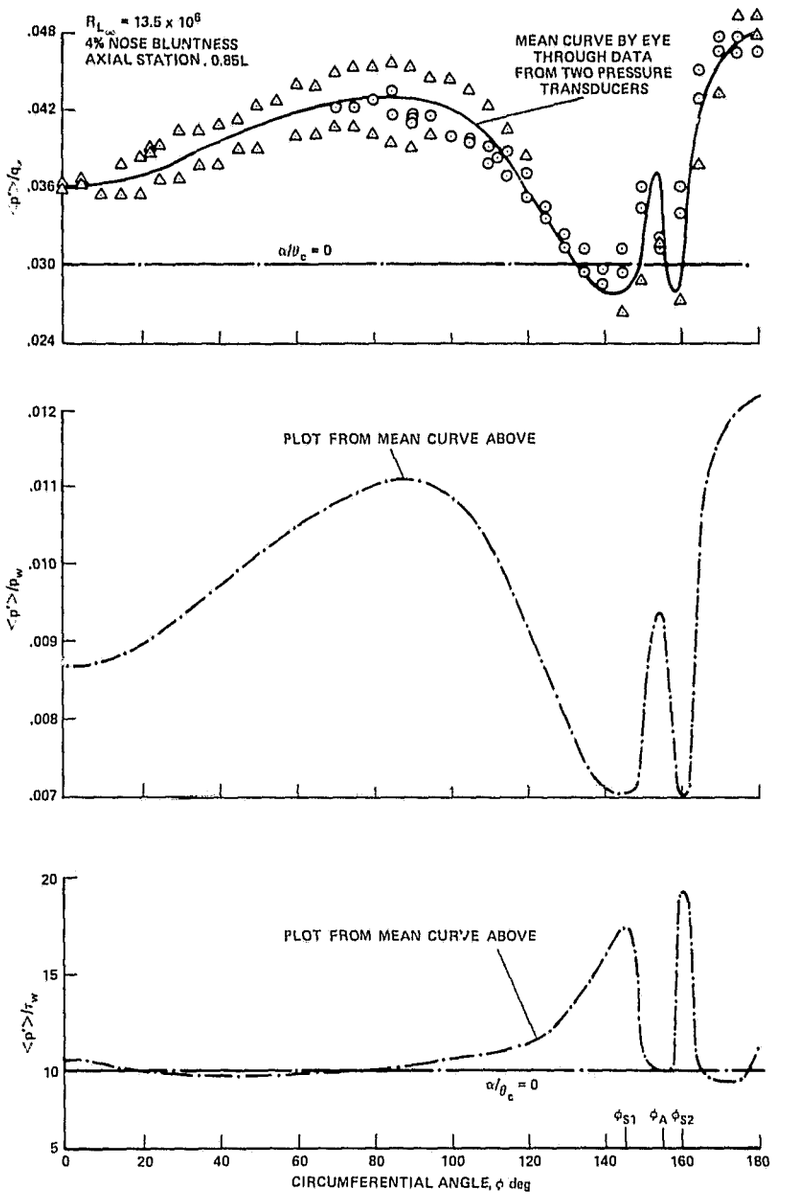

Fig. 15. RMS Pressures Around 5° Cone at $\alpha/\theta_c \sim 2.5$, $M_\infty = 0.6$.

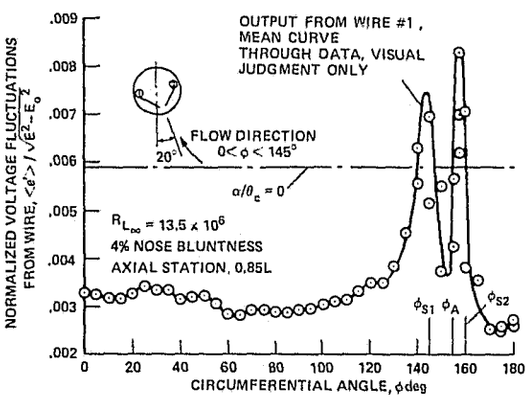

Fig. 16. RMS Voltages from Buried Wire on 5° Cone at $\alpha/\theta_c \sim 2.5$, $M_\infty = 0.6$.

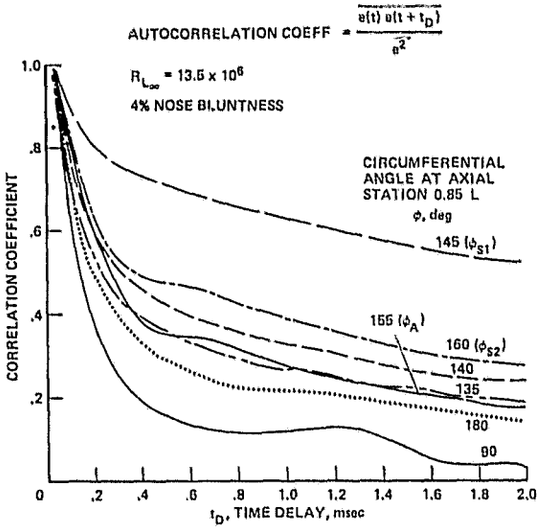

Fig. 17. Autocorrelations from Buried Wire at $\alpha/\theta_C \sim 2.5$, $M_\infty = 0.6$.

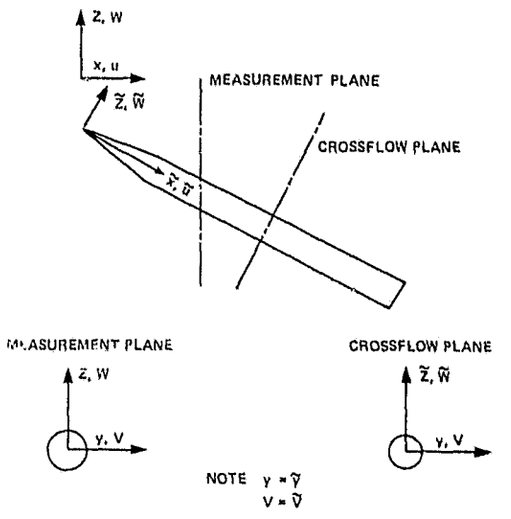

Fig. 19. Coordinate System about 16° Semiangle Tangent Ogive Cylinder.

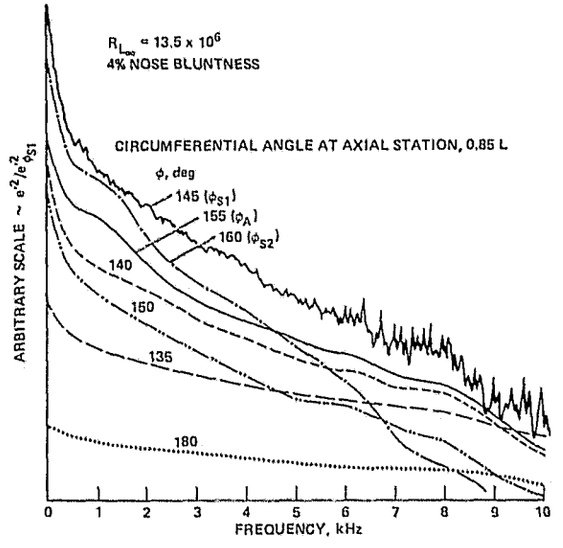

Fig. 18. Spectra from Buried Wire at $\alpha/\theta_C \sim 2.5$, $M_\infty = 0.6$.

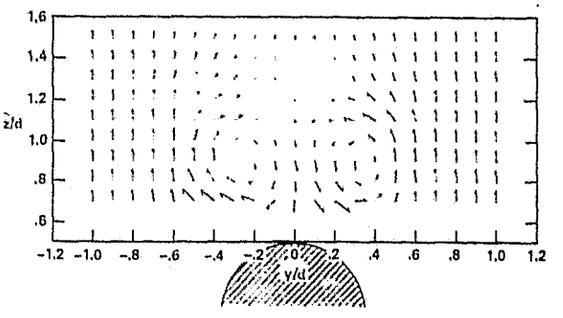

Fig. 20. Crossflow Velocity Vectors on Leeside of 16° Tangent Ogive Cylinder, $M_\infty = 0.6$, $\tilde{x}/d = 4$.

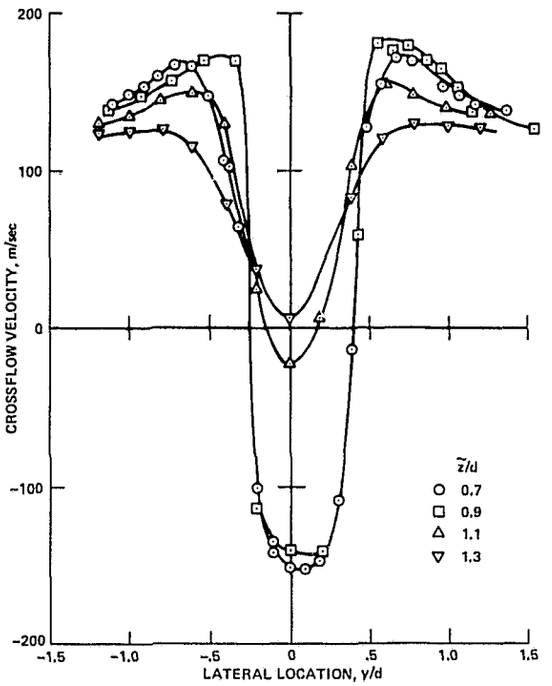

Fig. 21. Mean Vertical Velocity in Crossflow Plane of 16° Tangent Ogive Cylinder, M_∞ = 0.6, $\tilde{x}/d$ = 4.

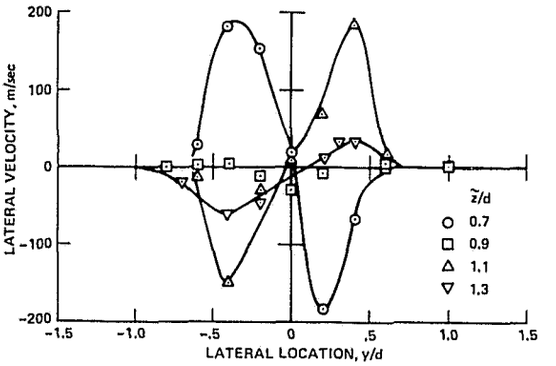

Fig. 23. Mean Lateral Velocity in Crossflow Plane about 16° Tangent Ogive Cylinder, M_∞ = 0.6, $\tilde{x}/d$ = 4.

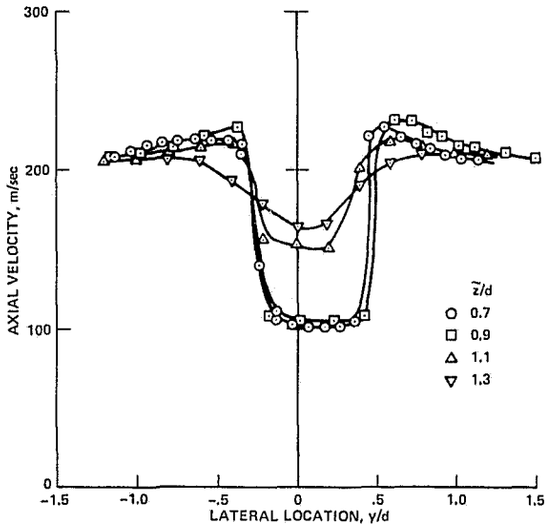

Fig. 22. Mean Axial Velocity in Wind-Tunnel Coordinates about 16° Tangent Ogive Cylinder, M_∞ = 0.6, $\tilde{x}/d$ = 4.

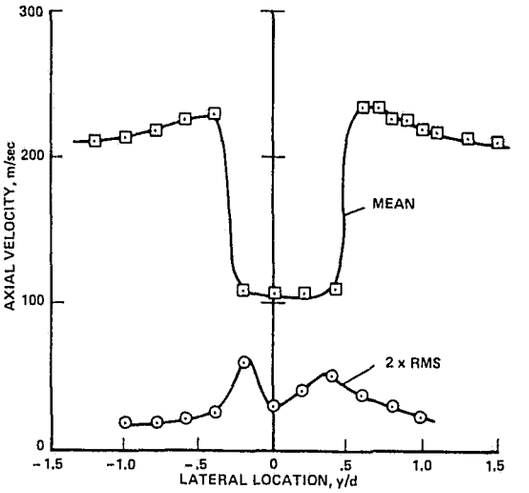

Fig. 24. Mean and RMS Axial Velocity about 16° Tangent Ogive Cylinder, M_∞ = 0.6, $\tilde{x}/d$ = 4, $\tilde{z}/d$ = 0.9.

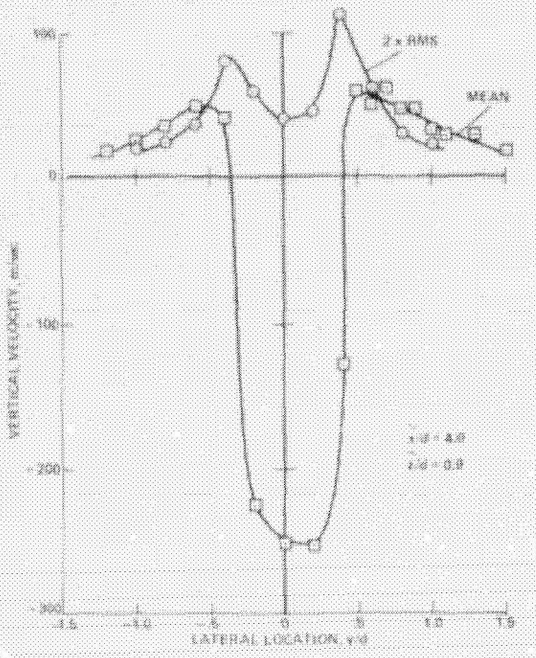

Fig. 25. Mean and RMS Vertical Velocity about 16° Tangent Ogive Cylinder, M_∞ = 0.6, x/d = 4, z/d = 0.9.

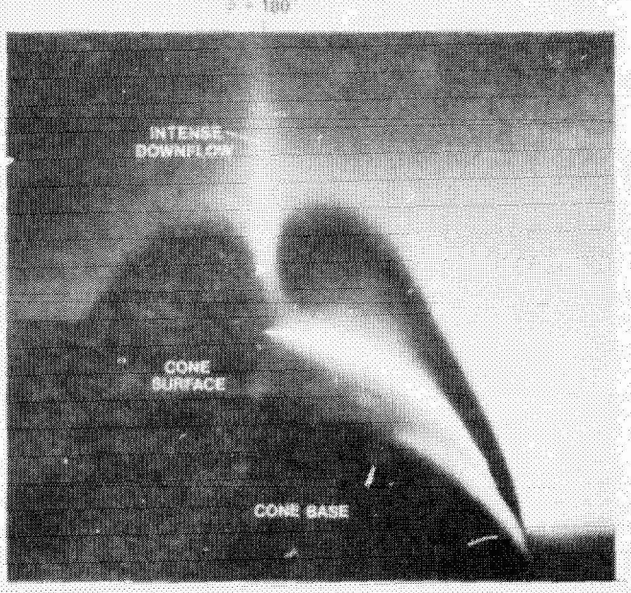

VIEW LOOKING UPSTREAM FROM CONE BASE

Fig. 26. Laser Vapor Screen of Nonsymetrical Lee-Side Flow Separation on 5° Cone at x/d_c = 2.9, M_∞ = 0.6.

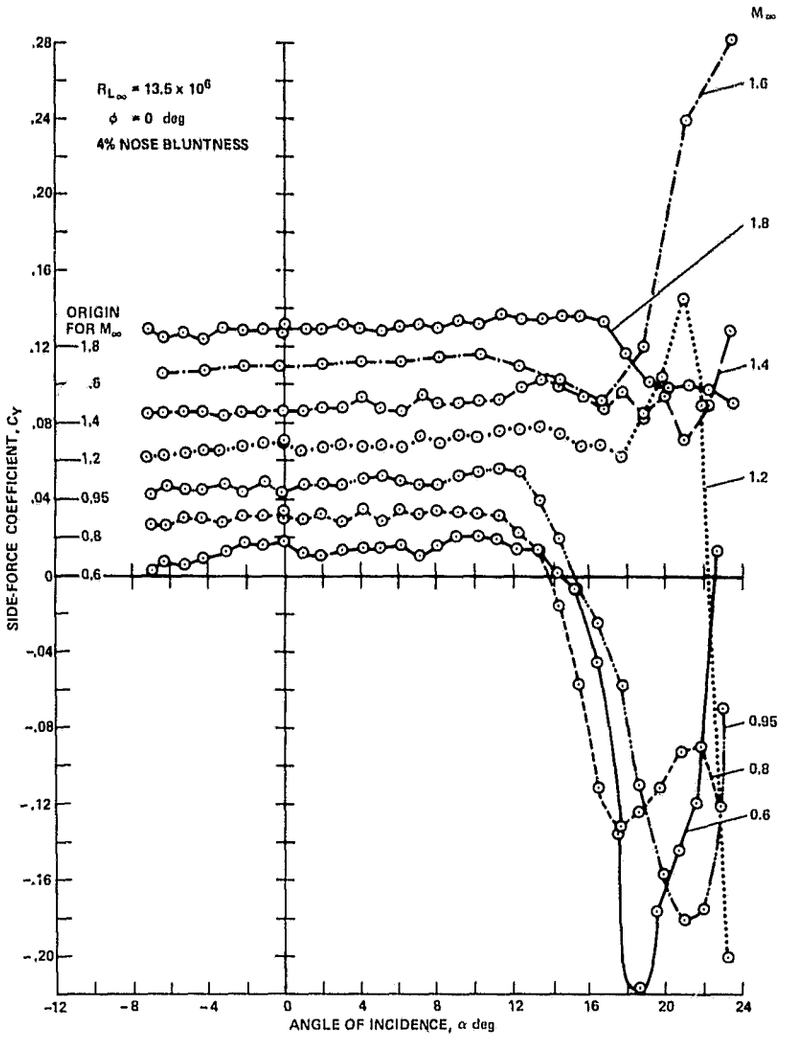

Fig. 27. Side Forces on 5° Cone for $0.6 < M_\infty < 1.8$.

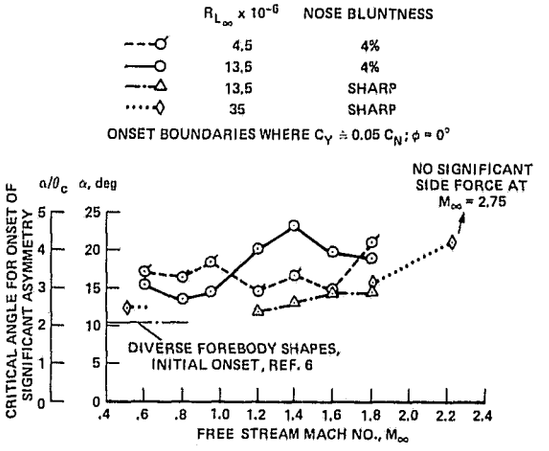

Fig. 28. Onset of Significant Side-Force Asymmetry for 5° Cone.

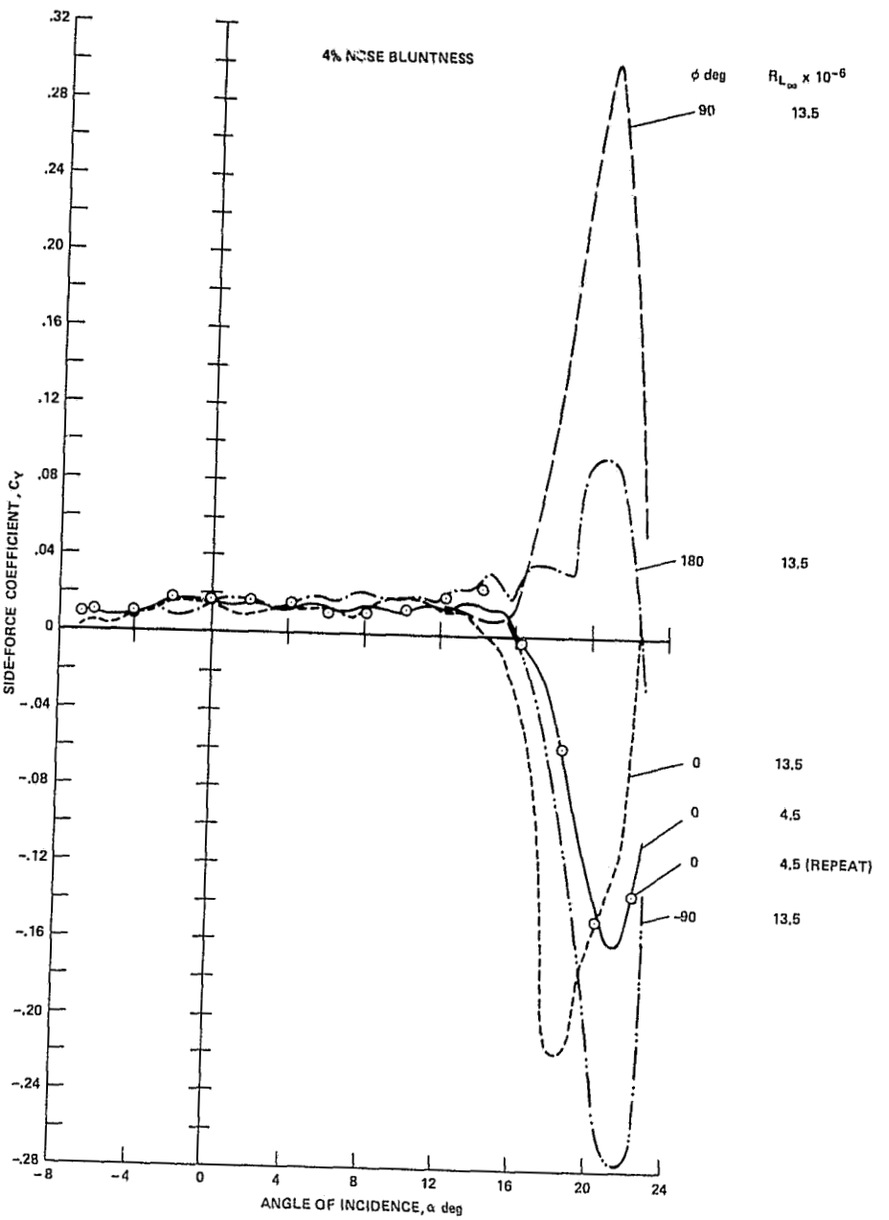

Fig. 29. Effect of Roll Angle and Reynolds Number on Side Force at $M_\infty = 0.6$.